PAPER

Check for updates

Unveiling the potential of low-strain nanoporous Li$_{0.33}$La$_{0.55}$TiO$_3$ nanofibers as a promising anode for Li-ion batteries: exploring the influence of carbon additives and binders

Ganeshbabu Mariappan, [ID] [a] Leonid Vasylechko, [ID] [b] Dharmalingam Kalpana [ID] [c] and Ramakrishnan Kalai Selvan [ID] [a]

Low-strain intercalation-type anodes are crucial for developing efficient, long-lasting, safe, and reliable lithium-ion batteries. Li$_{0.33}$La$_{0.55}$TiO$_3$ (LLTO) is one such anode gaining popularity; nevertheless, its preparation often involves long-term, high-temperature procedures. In this work, LLTO nanofibers were synthesized by electrospinning at different calcination temperatures (700 °C, 800 °C, and 900 °C) and compared with LLTO nanoparticles obtained by a sol–gel method. X-ray diffraction and Raman spectroscopic measurements revealed the presence of LLTO and electrochemically active La$_2$Ti$_2$O$_7$ and Li$_2$TiO$_3$ phases in the nanofibers. The interconnected LLTO nanoparticles form a porous structure within the fiber, which enhances the Li-ion (de)intercalation kinetics. Among the prepared samples, the LLTO nanofibers prepared at 800 °C exhibit better electrochemical properties than other variants, combining the conventional binder (PVDF) and carbon additives (carbon black). Furthermore, LLTO NFs calcined at 800 °C with the combination of Ketjenblack and sodium alginate (LLKS) provide a higher discharge capacity of 317 mAh g^{-1} than the Ketjenblack and PVDF (LLKB) (180 mAh g^{-1}) and conventional carbon black and PVDF (LLCP) (263 mAh g^{-1}) combinations at 0.1 A g^{-1} due to their low polarization and slightly increased pseudocapacitive contribution. Moreover, the carbon additive of Ketjenblack and the water-soluble sodium alginate binder improved the ionic conductivity, electrochemical activity, and reversibility. The diffusion kinetics of this electrode were examined using the GITT and EIS techniques, revealing a lower reaction resistance (0.85 Ohm g) and higher diffusion coefficient ($\sim 10^{-6}$ cm^2 s^{-1}). *Ex situ* XRD indicated that the unit cell volumes of the cycled LLCP, LLKP, and LLKS electrodes are comparable to those of the as-prepared LLTO nanofibers, with less than 1% volume expansion even after 1000 cycles, substantiating the strain-free nature and stability of the LLTO nanofibers.

1. Introduction

Identifying and exploring low-strain intercalation-type electrodes are mandatory for developing lithium-ion batteries with increased efficiency, longer lifespan, and improved safety. During Li-ion intercalation/de-intercalation, the conventional anode undergoes significant volumetric changes, creating mechanical strain and stress that lead to delamination, lithium dendrite formation, and thermal runaway.[1] On the other hand, low-strain intercalation-type oxide-based electrodes offer the

advantages of preventing dendrite growth for enhanced safety, improving electrical contact, boosting coulombic efficiency, promoting a stable and homogeneous SEI layer for long-term reliability, and minimizing volumetric changes to preserve mechanical integrity.[2,3] Therefore, various types of low-strain electrodes, including Li$_4$Ti$_5$O$_{12}$,[4] LiCrTiO$_4$,[5] LiY(MoO$_4$)$_2$,[6] LiAl$_5$O$_8$,[7] and Li$_{3.08}$Cr$_{0.02}$Si$_{0.09}$V$_{0.9}$O$_4$,[8] have been reported. Even though they have low-strain characteristics, their application in a full-cell configuration is constrained by either low specific capacity or higher operating potential, resulting in a lower energy density.

In contrast, lithium lanthanum titanate (LLTO) has gained potential interest due to its low strain feature, adequate operational potential, and decent specific capacity.[9] LLTO belongs to the perovskite-type (ABO$_3$) crystal structure. Here, the A site is occupied by both Li and La, whereas a Ti atom occupies the B site.[10] The ionic conductivity of LLTO ($\sigma = 10^{-5}$ to 10^{-3} S cm^{-1} @ RT) is

a Energy Storage and Conversion Devices Laboratory, Department of Physics,
  Bharathiar University, Coimbatore-641 046, Tamil Nadu, India.
  E-mail: selvankram@buc.edu.in

b Semiconductor Electronics Department, Lviv Polytechnic National University, 12
  Bandera Street, Lviv 79013, Ukraine. E-mail: leonid.o.vasylechko@lpnu.ua

c CSIR-Central Electrochemical Research Institute – Madras Unit, CSIR-Madras
  Complex, Chennai, 600113, India

mainly dependent on the size of the A-site ion (*i.e.*, La), the concentration of lithium ions and vacancies, and the nature of the B–O bond. Li-ion migration in LLTO occurs *via* the vacancy in the A site of the perovskite structure (ABO_3) and interstitial sites within the crystal lattice. The huge unoccupied area in the A site (18d and 6a positions) allows seamless Li-ion movements throughout the LLTO structure. Conversely, larger La ions expand and form a bottleneck, allowing the TiO_6 octahedra to tilt and rotate more freely, lowering the Li-ion activation energy. This facilitates the percolation of lithium ions.[11] Importantly, LLTO exhibits instability with lithium metal, which reduces Ti^{4+} to Ti^{3+}, substantially improving its electronic conductivity. This unique feature of transforming the electronic insulator into a conductor below 1.5 V *vs.* Li/Li^+ makes LLTO a promising anode for Li-ion batteries.[9]

Similarly, the conductive additive and binder also play a significant role in influencing the electrochemical performance. Therefore, carbonaceous elements are required to increase the electrical conductivity, given that most electrode materials are poor electronic conductors.[12] As a result, selecting the appropriate carbon additive is essential to achieve the desired performance. The binder also ensures adhesion with the current collector and is cohesive with the active material and conductive carbon, thereby contributing to the stability and cycle life of the electrode.[13] Given that the fluorinated polymer PVDF is recognized as a persistent organic pollutant, production and disposal may pose environmental risks. Hence, water-based binders with desired functionalities (hydrocolloid functional binders) are employed to avoid the use of PVDF and NMP.[14] Sodium alginate, a naturally occurring polymer obtained from brown algae, is a hydrocolloid functional binder. The biodegradable and ecologically benign properties of sodium alginate make it a viable option for binder applications in Li-ion batteries.[15] It is a valuable functional binder in the manufacturing of lithium-ion battery electrodes, providing binding and structural support and facilitating ion transport, mechanical reinforcement, and environmental benefits.

Over the years, numerous studies have explored the use of LLTO ($Li_xLa_yTiO_3$) as an electrode for lithium-ion batteries due to its structural integrity. Bohnke *et al.* obtained a capacity of 12 mAh g^{-1} at 0.34 mA g^{-1} by first employing solid-state synthesized LLTO as a positive electrode without any carbon additive.[16] Chen *et al.* reported that the specific capacity of $Li_{0.35}La_{0.55}TiO_3$ was 72 mAh g^{-1} (@0.0625 mA cm^{-2}), using 8 wt% acetylene black as a carbon additive and 8 wt% PVDF as the binder within an electrochemical window of 0 to 2 V *vs.* Li/Li^+. This capacity is attributed to the reversible (de)intercalation of 0.48 lithium ions per $La_{0.55}Li_{0.35}TiO_3$ formula unit, which is facilitated by vacancies at the A-site. Later, Hua *et al.* demonstrated a capacity of 145 mAh g^{-1} (@0.05 mA cm^{-2}) for $Li_{0.27}La_{0.54}TiO_{2.945}$ in the potential range of 0.01 to 2 V *vs.* Li/Li^+ and obtained an improved cycling performance by carbon coating (0.4%) through the chemical vapor deposition (CVD) technique.[17] Similarly, Zhang *et al.* prepared $La_{0.5}Li_{0.5}TiO_3$ anodes using a conventional solid-state approach, incorporating Ketjenblack (10 wt%) as a conductive additive and carboxyl methyl cellulose (10 wt%) as a binder. The prepared electrode

delivered 225 mAh g^{-1} at 0.1C/0.02 A g^{-1}, with good cycling stability over 3000 cycles. Furthermore, Keshu Dai *et al.* reported a reversible capacity of 270 mAh g^{-1} at 100 mA g^{-1} for a solid-state synthesized $Li_{0.2375}La_{0.5875}TiO_3$ electrode when combined with carbon black (30 wt%) and PVDF (10 wt%).[18] Overall, in the reports on the synthesis of LLTO, either solid-state or sol–gel techniques were used, which required high temperatures ($>1000\ °C$) for compound formation and particles with no specific morphology.[19] The calcination temperature plays a vital role in the phase purity of LLTO. It is often reported that $La_2Ti_2O_7$ and Li_2TiO_3 secondary phases are formed at low temperatures (below $1000\ °C$) and under lithium-deficient conditions. However, the electrochemical performance and lithium storage mechanism of mixed-phase LLTO have not been reported to date.
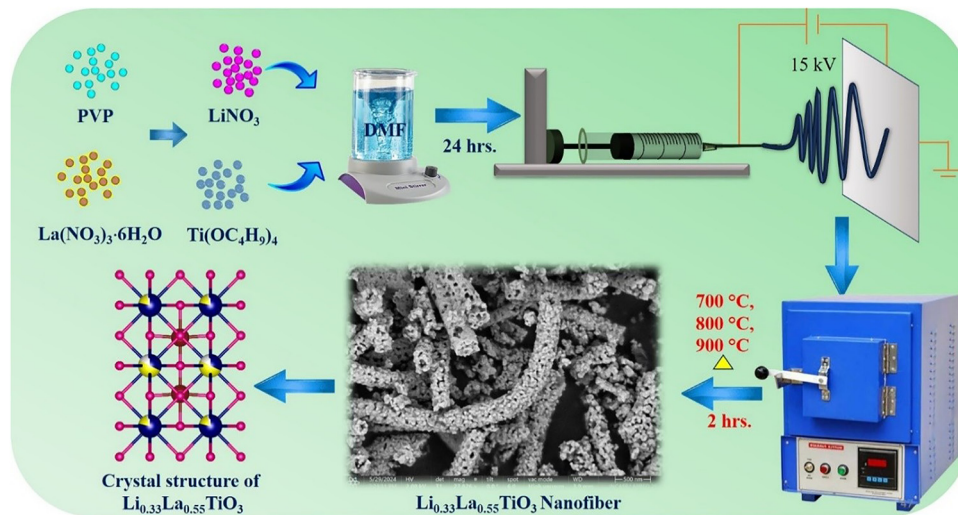
Conversely, the one-dimensional morphology created by electrospinning is beneficial for energy storage due to its porous nanofibers with huge surface area and interconnected structures, facilitating easy electrolyte penetration, enhancing the ionic transport, and improving the rate capability.[20–22] These nanofibers offer more active sites for electrochemical reactions due to their significantly higher surface area than bulk materials. They can accommodate greater volume changes during lithiation and delithiation while also experiencing lower mechanical stress, thereby enhancing the cycle life. Therefore, Zheng *et al.* examined the fast-charging characteristics of LLTO/carbon nanofibers prepared using the electrospinning technique and calcined at $900\ °C$ in an inert atmosphere,[23] which yielded a maximum capacity of 250 mAh g^{-1} (0.2C/0.04 A g^{-1}). Along this line, the present work concentrated on synthesizing low-strain anode $Li_{0.33}La_{0.55}TiO_3$ nanofibers at low temperatures of $700\ °C$, $800\ °C$, $900\ °C$ in an air atmosphere and examined the intercalation behavior of Li-ions using an alternative hydrocolloid functional binder (sodium alginate) and conductive additive (Ketjenblack) compared to conventional materials (PVDF/carbon black). According to the results, it was elucidated that LLTO with Ketjenblack and sodium alginate binder is the better choice for improved electrochemical performance with limited volume expansion (0.7%) even after 1000 cycles.

2. Experimental methods and materials

2.1. Synthesis of the $Li_{0.33}La_{0.55}TiO_3$ (LLTO) nanofibers

For the synthesis of the $Li_{0.33}La_{0.55}TiO_3$ (LLTO) nanofibers by the electrospinning technique, polyvinylpyrrolidone (PVP) was used as a carrier/sacrificial compound. Stoichiometric amounts of lithium nitrate ($LiNO_3$-3.3 mM), lanthanum(III) nitrate hexahydrate ($La(NO_3)_3·6H_2O$-5.6 mM), and titanium butoxide ($Ti(OC_4H_9)_4$-10 mM) were dissolved in 20 mL of DMF containing 15% acetic acid ($C_2H_4O_2$) and agitated for 30 min to produce a homogenous product. Further, 2 g of PVP was gradually added to the above-mentioned mixture and stirred for 12 h. Subsequently, the polymer solution was electrospun

Scheme 1 Schematic of the synthesis of the LLTO nanofibers.

over aluminum foil at a voltage of 15 kV and flow rate of 0.6 mL h^{-1}. During the spinning process, the needle and plate were held at a distance of 15 cm. Finally, the polymer mat was calcined in air at 700 °C (LLTO NF-700), 800 °C (LLTO NF-800), and 900 °C (LLTO NF-900) for 3 h. Similarly, LLTO nanoparticles were prepared using the same precursor solution, initially fired at 300 °C, followed by grinding and further calcination at 800 °C (LLTO NP-800). A schematic representation of the experimental procedure is given in Scheme 1.

2.2 Electrode preparation and coin cell assembly

The negative electrode was prepared by coating the active material (LLTO), binder (PVDF/sodium alginate), and conductive carbon (carbon black/Ketjenblack) at a ratio of 70 : 20 : 10 in the desired solvent (N-methylpyrrolidine/double distilled water) on a Cu substrate using the doctor blade technique. The coated Cu substrate was allowed to dry overnight at 80 °C. The electrodes were punched into 12 mm diameter round discs, with an active material loading of 1 mg cm^{-2}. Subsequently, CR2032-type coin cells were assembled in an Ar-filled glove box (H$_2$O < 0.5 ppm, O$_2$ < 0.5 ppm). The working electrode was an LLTO-coated Cu substrate, while the counter and reference electrodes were Li chips (2 mm) separated by a glass fiber separator. 1 M LiPF$_6$ mixed with EC-DMC (1 : 1 volume ratio) was utilized as the electrolyte.

2.3. Characterization techniques

X-ray diffraction analysis was performed using a Bruker D8 Advance diffractometer with a Cu Kα source at a wavelength of 1.5418 Å. Raman spectra were obtained using a Horiba LAB-RAM HR instrument with a 532 nm laser. Field-emission scanning electron microscopy images were analyzed using an APREO 2S instrument. High-resolution microscopic images (HRTEM), selected area diffraction patterns (SAED), and elemental mapping of LLTO NFs were studied using a JEOL-JEM-2100 plus microscope attached to an Oxford EDS instrument.

Galvanostatic charge–discharge (GCD) cycling was performed using a multichannel WonAtech instrument in the potential range of 0 to 3 V vs. Li/Li$^+$. Cyclic voltammetry (CV) was performed using a Biologic electrochemical workstation at different scan rates. The charge transfer kinetics of the constructed cell, both before and after cycling at open-circuit potential (OCP), were investigated via electrochemical impedance spectroscopy (EIS) measurements on a Biologic SP-150 workstation. A 10 mV perturbation voltage was applied over the frequency range of 1 mHz to 1 MHz.

3. Results and discussion

3.1 Structural properties

The XRD patterns of LLTO NFs (700, 800, and 900) and LLTO NPs (Fig. 1a) indicate the formation of the tetragonal Li$_{0.33}$La$_{0.55}$TiO$_3$ phase, which aligns well with the standard JCPDS Card (no: 01-087-0935), belonging to the P4/mmm space group. The prominent peaks in their XRD patterns confirm the primary phase of Li$_{0.33}$La$_{0.55}$TiO$_3$. However, LLTO NF-800 has additional phases of La$_2$Ti$_2$O$_7$ and Li$_2$TiO$_3$, which are indexed with symbols (*) and (#), respectively.[24,25] The relative quantities of these mixed phases were estimated, with Li$_2$TiO$_3$ (PDF-2 card 33-831) comprising ∼5–10% of the sample and La$_2$Ti$_2$O$_7$ (PDF-2 card 28-517) constituting around 15%. Furthermore, a minor phase of hydrated La$_{0.66-x}$TiO$_{3-3x}$(OH)$_3$ (PDF-2 card 51-123), representing about 5%, was also detected and cannot be neglected in the overall composition of LLTO NF-800. The lattice parameters and unit cell volume of LLTO NFs and LLTO NPs are listed in Table 1. The nanofiber samples (LLTO NF) show a gradual decrease in lattice parameter 'a' from 3.897 Å at 700 °C to 3.8677 Å at 900 °C, while the 'c' parameter remains relatively stable around 7.77–7.78 Å. Correspondingly, the unit cell volume decreases from 118.0 Å^3 to 116.19 Å^3 as the calcination temperature increases. LLTO NP-800 exhibits slightly lower lattice parameters and a reduced unit cell volume
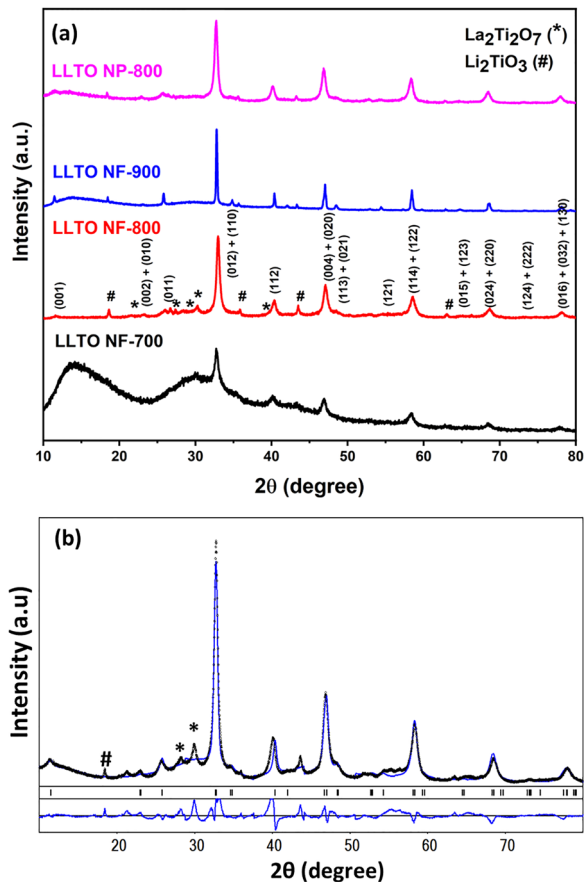
Fig. 1 (a) XRD patterns of LLTO NF-700, LLTO NF-800, LLTO NF-900, and LLTO NP-800. (b) Rietveld refinement of LLTO NF-800.

Table 1 Lattice parameters of LLTO NFs and LLTO NPs

Material	$a = b$ (Å)	c (Å)	V (Å^3)
LLTO NF-700	3.897(5)	7.77(2)	118.0(5)
LLTO NF-800	3.882(1)	7.785(5)	117.3(2)
LLTO NF-900	3.8677(4)	7.7672(9)	116.19(4)
LLTO NP-800	3.876(1)	7.778(3)	116.9(1)

(116.9 Å^3) compared to LLTO NF-800 (117.3 Å^3), indicating a marginally denser crystal structure. Full-profile crystal structure refinement was performed for LLTO NF-800 (Fig. 1b) using the Rietveld method, applying the tetragonal $P4/mmm$ structural model reported for $(La_{1.12}Li_{0.62})(Ti_2O_6)$ by Ruiz *et al.*[26] The refinement of the main perovskite phase demonstrates moderate agreement between the calculated and experimental diffraction profiles, with minimal residuals of $R_I = 0.0866$ and $R_p = 0.2793$ (Fig. 1b). The structural model of LLTO suggests an uneven distribution of La^{3+} along the c-axis within the two adjacent A-sites (or cages) of the perovskite lattice. This unequal distribution of La^{3+} results in the doubling of the c-axis lattice parameter, giving rise to superstructure lines in the diffraction pattern. This finding indicates that the perovskite structure is composed of alternating La^{3+}-rich and La^{3+}-poor layers along the c-axis, which contribute to the unique structural characteristics of LLTO.[27,28]

Examination of the XRD pattern of LLTO NF-900 revealed a cation-deficient perovskite phase close to the $Li_{0.485}La_{0.505}TiO_3$ and $Li_{0.125}La_{0.625}TiO_3$ compositions presented in the ICDD PDF-2 database (PDF-2 cards 46-466 and 47-669), as well as cubic spinel $Li_4Ti_5O_{12}$ ($Li_{4/3}Ti_{5/3}O_4$) phase (PDF-2 cards 26-1198 and 72-427) in the amount of 7.0 wt%, as derived by further quantitative full-profile Rietveld refinement (Fig. S1a). As a starting model for refinement, the atomic positions in the tetragonal $La_{1.12}Li_{0.62}Ti_2O_6$ ($La_{0.56}Li_{0.31}TiO_3$) structure, which were derived by Ruiz *et al.*[26] from neutron diffraction data, as well as in the cubic $Li_{1+x}Ti_{2-x}O_4$ ($x = 0.33$) spinel structure[29] were used. In the refinement procedure, the phase percentage and lattice parameters of both phases were derived after corrections for absorption and instrumental sample shift. In the case of the main perovskite phase, the coordinates, atomic displacement parameters, and the occupation of two nonequivalent positions 1a (0, 0, 0) and 1b (0, 0, 1/2) by lanthanum ions and the two-fold octahedral 2h site by titanium ions were also refined. Lithium contribution was not considered in this analysis due to the extremely low X-ray scattering factor of Li$^+$ ions. Sequential optimisation of the profile and structural parameters yielded an excellent fit between the calculated diffraction profiles and the experimental XRD data (Fig. S1a), with the final structural parameters and residuals presented in Table S1. The graphical results of two-phase Rietveld refinement shown in Fig. S1a prove the presence of 93.0% $Li_{0.33}La_{0.55}TiO_3$ perovskite (blue) and 7.0% of $Li_4Ti_5O_{12}$ spinel (red) phases in LLTO NF-900. The experimental XRD pattern after elimination of the diffuse maxima of amorphous component (small black circles) is shown in comparison with the calculated profiles of the perovskite and spinel phases. The difference between the measured and computed profiles is shown as a curve below the diagrams. Short vertical bars indicate the positions of the diffraction maxima in the perovskite and spinel phases.

According to Table S1, it was proven that La ions exhibit a clear preference for the 1a (0, 0, 0) position with respect to (0, 0, 1/2). The total La contents derived from the Rietveld analysis ($La_{0.545}$) closely match the nominal $Li_{0.33}La_{0.55}TiO_3$ composition. The location of the Li$^+$ ion, as shown in Table S1, was determined based on neutron diffraction[26] and ^{7}Li NMR data,[30] revealing a peculiarity in the distribution of lithium in both positions. Rather high values of displacement parameters $B_{iso/eq}$ were obtained for the O1 and O2 atoms in the 4i and 1c sites (Table S1), indicating a possible deficiency at both of these oxygen sites in the studied $Li_{0.33}La_{0.55}TiO_3$ structure. The formation of oxygen-deficient perovskites, specifically $La_{2/3-x}TiO_{3-3x/2}$, was reported by Bhuvanesh.[31] The comparison of the lattice parameters of the studied $Li_{0.33}La_{0.55}TiO_3$ material with the literature data for the $La_{2/3-x}Li_{3x}TiO_3$ series with $x = 0.03–0.167$ shows its similarity with the $x = 0.104$ composition, lying on the border between orthorhombic ($x \leq 0.073$) and tetragonal ($x \geq 0.104$) cation-deficient perovskites.
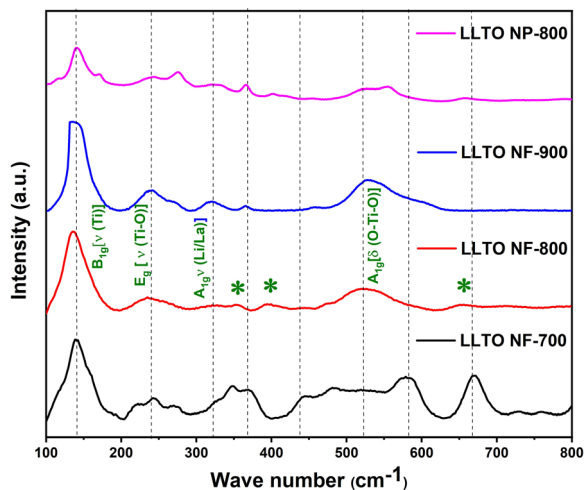
Fig. 2 Raman spectra of LLTO NF-700, LLTO NF-800, LLTO NF-900, and LLTO NP-800.

The Rietveld refinement of LLTO NP-800 (Fig. S1b) reveals a phase composition similar to that of LLTO NF-900, consisting of cation-deficient perovskite, minor amounts of spinel phases, and an amorphous phase. The major difference lies in the significant line broadening of the main $Li_{0.33}La_{0.55}TiO_3$ perovskite phase, which does not allow precise structural analysis of the material (note that the peaks of the parasitic $Li_4Ti_5O_{12}$ phase remain relatively narrow). Additionally, full-profile Rietveld refinement revealed some additional features of the patterns, such as extra left-side intensity near the (112) Bragg's peak at $\sim 40°$ (Fig. S1b), which cannot be modeled within the framework of two constituent structures. This point concerns the possible presence of an unidentified phase in the material. The additional phases present in LLTO NFs and LLTO NPs are listed in Table S2.

The Raman spectra of LLTO NF-700, LLTO NF-800, LLTO NF-900, and LLTO NP-800 (Fig. 2) reveal multiple high-intensity peaks, which correspond to the Raman-active vibrational modes of the tetragonal lattice structure of LLTO. The spectra contain several characteristic vibrational modes associated with the bonding environment of the material. Specifically, the peaks centered at 136 cm^{-1}, 234 cm^{-1}, and 524 cm^{-1} are associated with the $3E_g$ vibrational mode, reflecting the dynamic behavior of the atoms within the tetragonal framework. The prominent peak at 136 cm^{-1} is attributed to the vibration of titanium cations within the a–b plane of the LLTO structure. This motion correlates with the displacement of oxygen atoms within the lattice. The high intensity of this peak suggests a strong coupling between the titanium and oxygen atoms, highlighting the structural integrity of the tetragonal lattice and its contribution to the overall stability of the material. In addition to the Ti-centered vibrations, the Raman peaks observed at 234 cm^{-1} and 524 cm^{-1} correspond to specific cation displacements within the LLTO framework. The peak at 234 cm^{-1} is linked to the E_g vibrational mode, representing the displacement of A-site cations, such as La and

Li, while the peak at 524 cm^{-1} is attributed to the A_{1g} mode, which arises from the stretching of Ti–O bonds and the bending of O–Ti–O linkages. These modes provide valuable information about the interaction between the titanium and oxygen sublattices, indicating the flexibility and vibrational dynamics of the LLTO structure. The presence of these peaks supports the notion that the Ti–O framework in LLTO plays a key role in its ionic conductivity. Notably, a peak at 320 cm^{-1} is observed in the spectrum, which is assigned to the A_{1g} mode of the Li/La vibrations along the c-axis of the tetragonal structure.[32,33] This peak highlights the vibrational coupling between the Li and La ions, further confirming their roles as A-site cations in the LLTO lattice. The broad nature of this peak suggests a certain degree of disorder or variability in the vibrational environment along the c-axis, which may arise from slight variations in the positioning or coordination of Li and La ions within the structure. This could have implications for the ion transport properties of the material, given that cation displacement along the c-axis may influence the lithium-ion mobility within the solid matrix. In addition to the peaks attributed to LLTO, the Raman spectra also reveal additional peaks at 353 cm^{-1}, 394 cm^{-1}, and 652 cm^{-1}, marked by asterisks (*). These characteristic peaks correspond to the Raman spectra of lithium titanate (Li_2TiO_3), and the secondary phase observed in the XRD analysis.[34] The presence of these peaks suggests that a small fraction of Li_2TiO_3 was formed during the synthesis process, coexisting with the primary LLTO phase. Although the formation of this secondary phase may slightly alter the overall performance of the material, it is likely that the dominant LLTO phase still governs the primary electrochemical behavior. Therefore, the Raman analysis provides a comprehensive understanding of the structural and compositional intricacies of the LLTO nanofibers.

3.2 Morphological properties

Fig. 3 represents the FE-SEM images and EDS spectra of the LLTO samples synthesized under different conditions. Fig. 3(a) and (b) show the FE-SEM images of LLTO NF-700, where this sample displays an interconnected network of nanofibers with a relatively smooth surface spotted by fine nanograins, indicating that the fibrous one-dimensional morphology is preserved under these conditions. The average diameter of LLTO NF-700 was determined to be 150 nm. When the calcination temperature was increased to 800 °C, as shown in Fig. 3(d) and (e) for LLTO NF-800, the fiber network persisted, but the individual fibers became rougher. They are covered with larger and more nanograins, indicating clear evidence of grain growth with an average diameter of 141 nm. At an even higher temperature of 900 °C, corresponding to Fig. 3(g) and (h) for LLTO NF-900, the nanofiber network became increasingly porous, and the fibers display distinct grain boundaries and coarser surfaces; here, the average diameter substantially increases to 311 nm, reflecting grain coalescence and a diminished fiber definition. In contrast, Fig. 3(j) and (k) depict LLTO NP-800, where the material appears as compact, densely packed aggregates of spherical or sub-spherical particles with an average diameter
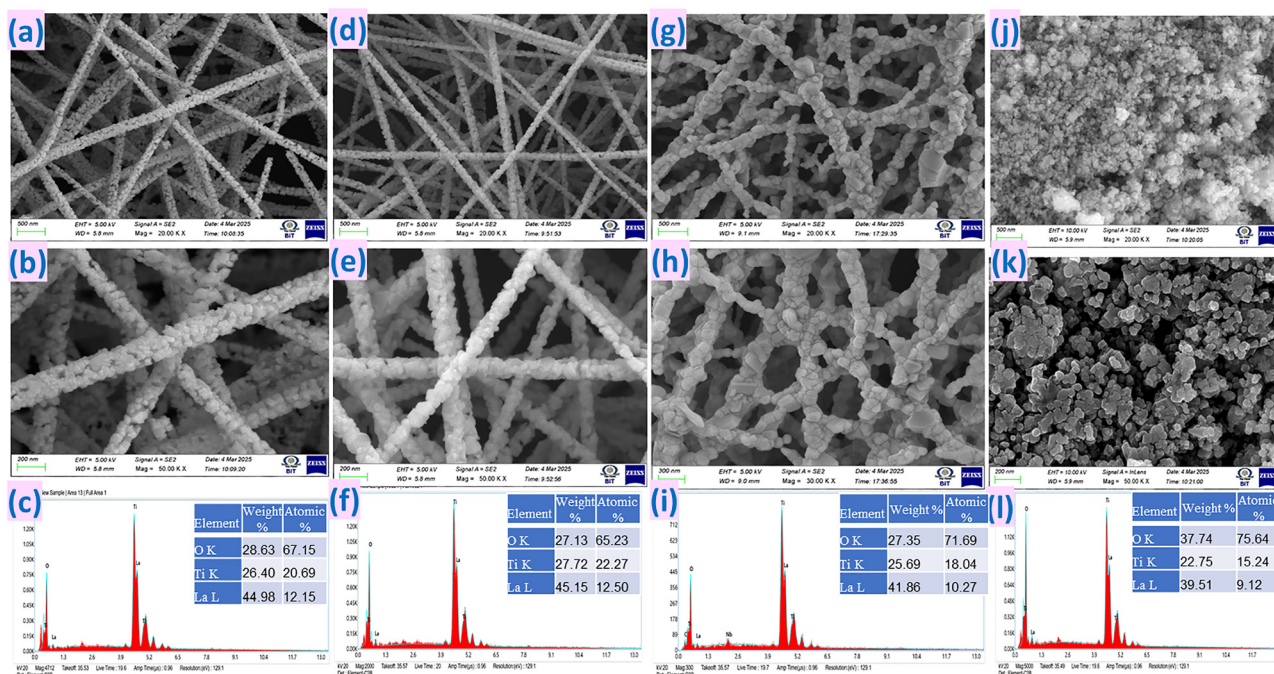
Fig. 3 FE-SEM images of (a) and (b) LLTO NF-700, (d) and (e) LLTO NF-800, (g) and (h) LLTO NF-900, and (j) and (k) LLTO NP-800. (c), (f), (i) and (l) EDS spectra of the corresponding LLTO samples (inset: elemental composition).

of 70 nm. As the temperature increases, the nanofiber samples transition from well-defined, continuous fibers to coarser, porous structures, while nanoparticles form tightly clustered, non-fibrous agglomerates. These morphological differences, driven by both the synthesis method and calcination temperature, can critically affect the functional and electrochemical properties of the material. The corresponding EDS spectra and elemental composition for each sample are provided in Fig. 3(c), (f), (i) and (l). The presence of lanthanum (La), titanium (Ti), and oxygen (O) was confirmed in all the samples, consistent with the LLTO composition. The atomic and weight percentage data indicate that with an increase in annealing temperature, there is a gradual increase in La content and a slight decrease in Ti and O content, potentially due to the loss of oxygen during high-temperature processing. The LLTO NP-800 sample exhibits a relatively higher oxygen content, which is possibly attributed to the increased surface oxidation in the nanoparticle morphology.

The representative HR-TEM images (Fig. 4(a)–(c)) of LLTO NF-800 provide further insight into its nanofiber structure at the nanoscale. The nanofibers, with an average diameter of 500 nm, are composed of interconnected cuboid-shaped nanoparticles, measuring 50 to 80 nm in size. The HR-TEM image (Fig. 4c) reveals lattice fringes corresponding to the (101) plane of LLTO, confirming the crystallinity of the nanofibers. The interconnected nature of these nanoparticles likely contributes to the mechanical stability and conductivity of the fibers, making them suitable candidates for Li-ion batteries. These nanoparticles form polycrystalline fibers, as evidenced by the SAED pattern (Fig. 4d), which shows concentric rings with

bright spots. Furthermore, the elemental composition of the fibers was examined using STEM and elemental mapping (Fig. 4(e)–(j)). The elemental maps demonstrate the uniform distribution of La, Ti, and O throughout the fiber structure. The homogeneous elemental distribution is crucial for maintaining consistent electrochemical properties across the material. The absence of phase separation or aggregation of elements suggests that the synthesis method was effective in creating a well-dispersed and stable material. This uniform elemental distribution, combined with the structural features of the nanofibers, indicates that these LLTO nanofibers have significant potential for application as anodes in lithium-ion batteries, offering both structural stability and enhanced electrochemical performance.

3.3 Electrochemical properties of LLTO NFs and NPs

To investigate the electrochemical characteristics of LLTO NFs and LLTO NPs as anodes, CR2032 coin cells were fabricated. Fig. 5a shows their measured CV curves in the potential range of 0–3 V vs. Li/Li$^+$ at a scan rate of 0.5 mV s^{-1}. They consist of several redox peaks in the potential window of 0–1.8 V vs. Li/Li$^+$, which are attributed to the multiple-phase transitions of Ti^{4+} ions in LLTO NFs.[35] Specifically, the prominent redox peaks at 1.52 and 1.63 V vs. Li/Li$^+$ (for LLTO NF-800) are attributed to the redox reactions of Ti^{3+}/Ti^{4+}.[17] The potential difference (ΔV) between the Ti^{3+}/Ti^{4+} redox couple for LLTO NF-700, LLTO NF-800, LLTO NF-900, and LLTO NP-800 is 146 mV, 113 mV, 173 mV, and 152 mV, respectively. Notably, LLTO NF-800 exhibited the lowest polarization, indicating enhanced electrochemical kinetics. Additionally, LLTO NF-800 exhibited the
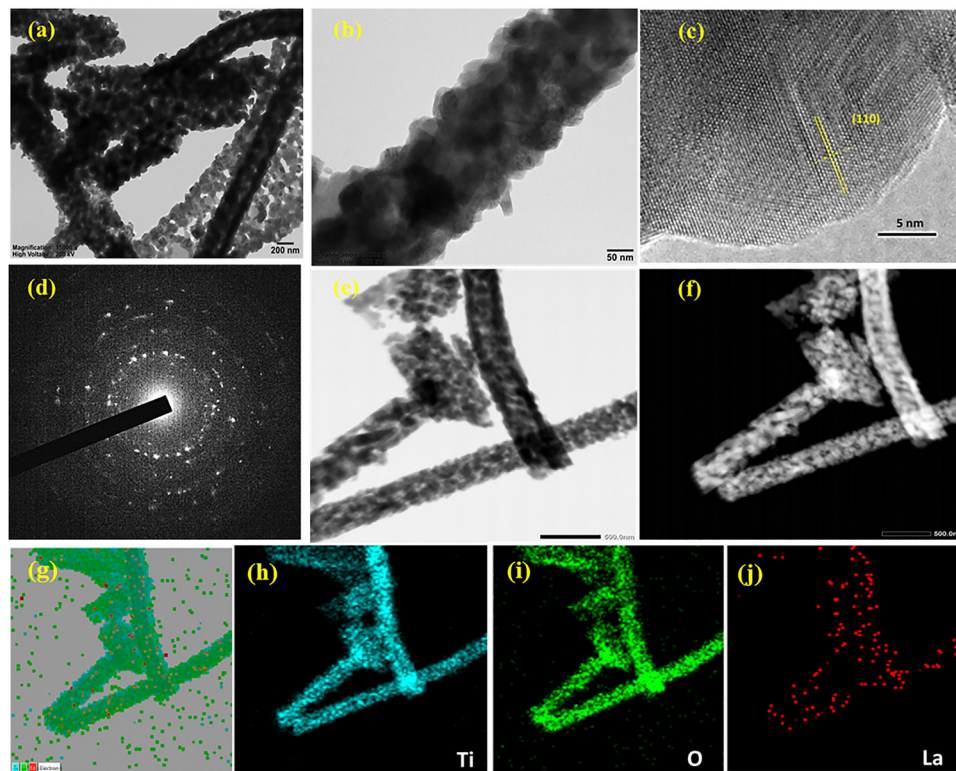
Fig. 4 (a)–(c) HR-TEM image, (d) SAED pattern, (e) and (f) bright and dark field images, and (g)–(j) elemental mapping of LLTO NF-800.

highest current response, underscoring its superior electrochemical properties for lithium storage. Furthermore, the galvanostatic charge–discharge (GCD) analysis was performed for LLTO NF-700, LLTO NF-800, LLTO NF-900, and LLTO NP-800 at a current density of 0.1 A g^{-1}. As depicted in Fig. 5b, the GCD profiles of LLTO NFs reveal that lithiation (discharge) starts near 1.5 V $vs.$ Li/Li^{+}, followed by a well-defined plateau at around 1.55 V $vs.$ Li/Li^{+} and a gradual sloping process down to 0 V. The similar plateau observed at 1.62 V $vs.$ Li/Li^{+} during the charging process aligns with the CV results, confirming the intercalation/deintercalation of Li-ions and the Ti^{3+}/Ti^{4+} reaction. Among the LLTO NF electrodes, LLTO NF-800 exhibits the highest capacity ($\sim$175 mAh g^{-1}) with a broad plateau, indicating its enhanced lithium storage.

Fig. 6(a)–(d) illustrate the GCD profiles of the LLTO NF-700, LLTO NF-800, LLTO NF-900, and LLTO NP-800 electrodes, respectively, measured at various current densities ranging from 0.1 A g^{-1} to 2 A g^{-1}. At lower current densities, all the electrodes exhibit higher specific capacities due to their longer charge–discharge durations, which facilitate complete lithium-ion intercalation and de-intercalation, respectively. Conversely, as the current density increases, a gradual decline in capacity is observed for all the cells. This reduction is attributed to the increased polarization and kinetic limitations, which hinder efficient lithium-ion transport and insertion/extraction processes. Among the electrodes, LLTO NF-800 (Fig. 6b) consistently delivers the highest discharge capacity across all current rates, signifying its superior electrochemical performance.

Specifically, at a high current density of 2 A g^{-1}, the discharge capacities of LLTO NP-800, LLTO NF-700, LLTO NF-800, and LLTO NF-900 are 16 mAh g^{-1}, 26 mAh g^{-1}, 68 mAh g^{-1}, and 40 mAh g^{-1}, respectively. The significantly enhanced capacity of LLTO NF-800 at this rate highlights its improved rate capability and lithium storage performance, likely stemming from its optimized nanostructure, which promotes efficient lithium-ion diffusion and electron transport. In contrast, LLTO NP-800 shows the lowest capacity, reflecting the limitations associated with its particular morphology under high-rate conditions. Fig. 6(e)–(h) present the differential capacity (dQ/dV) plots, which provide insight into the redox reactions occurring during the charge–discharge process. All the electrodes exhibit characteristic peaks at around 1.6 V $vs.$ Li/Li^{+}, corresponding to the reversible Ti^{3+}/Ti^{4+} redox couple, confirming effective lithium-ion intercalation and deintercalation. At higher current densities, these peaks exhibit slight shifts in potential, indicative of polarization effects. Notably, the LLTO NF-800 (Fig. 6f) and LLTO NF-900 (Fig. 6g) electrodes display sharper and more pronounced redox peaks compared to LLTO NF-700 (Fig. 6e) and LLTO NP-800 (Fig. 6h), suggesting their enhanced electrochemical kinetics and better redox reaction reversibility.

Fig. 7a represents the rate capability of the various LLTO electrodes measured at different current densities. At 0.1 A g^{-1}, all the electrodes exhibit high capacities, indicating facile lithium-ion intercalation. However, a substantial decrease in capacity was observed for all the samples when the current density increased to 2 A g^{-1}. Notably, LLTO NF-800 retained a
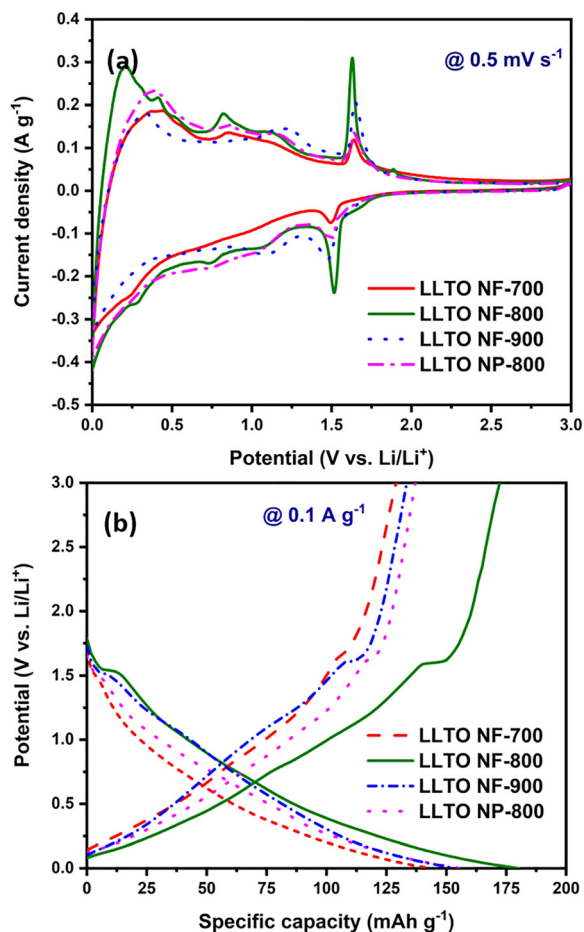
Fig. 5 (a) CV measured at 0.5 mV s^{-1} and (b) GCD at 0.1 A g^{-1} for LLTO NFs and LLTO NPs.

significantly higher capacity (68 mAh g^{-1} at 2 A g^{-1}) compared to LLTO NF-700 (31 mAh g^{-1} at 2 A g^{-1}), LLTO NF-900 (41 mAh g^{-1} at 2 A g^{-1}), and LLTO NP-800 (13 mAh g^{-1} at 2 A g^{-1}).

This improved performance suggests that the optimized nanostructure of LLTO NF-800 facilitates enhanced lithium-ion diffusion. Upon returning the current density to 0.1 A g^{-1}, LLTO NF-800 recovers a specific capacity of 152 mAh g^{-1}, representing 92% retention of its initial value in the 10th cycle. Following the rate performance, the electrodes were subjected to 200 continuous cycles at a current density of 1 A g^{-1} (Fig. 7b). The discharge capacities and capacity retention after 200 cycles were as follows: LLTO NF-700, 63 mAh g^{-1} (113%); LLTO NF-800, 102 mAh g^{-1} (99%); LLTO NF-900, 97 mAh g^{-1} (103%); and LLTO NP-800, 53 mAh g^{-1} (91%).

Fig. 8 shows the Nyquist plots measured at OCV for the LLTO NF-700, LLTO NF-800, LLTO NF-900, and LLTO NP-800 cells at frequencies ranging from 1 MHz to 1 mHz with an AC voltage of 10 mV. The Nyquist plot of the LLTO electrodes contains a semicircle at higher frequencies, followed by a low-frequency Warburg tail. The intercepts on the horizontal axis indicate the resistance of the organic electrolyte. At the same time, the flat arc in the mid-frequency range corresponds to the charge-transfer resistance at the electrode/electrolyte interface. The flattened arc in the high-frequency range is generally considered to be closely related to ion transport through the SEI, coupled with the double-layer capacitance. Lithium-ion diffusion in the crystal lattice is associated with the linear component of the Warburg impedance. The equivalent circuit model of the LLTO electrodes is comprised of several key elements that represent different electrochemical processes. R_s corresponds to the solution resistance (electrolyte resistance), appearing as the initial intercept on the real axis of the Nyquist plot. R_{ct} (charge transfer resistance) is associated with the diameter of the semicircle and reflects the kinetics of Li-ion intercalation/de-intercalation, where a lower value indicates faster charge transfer. CPE2 (constant phase element) models the non-ideal capacitance at the electrode–electrolyte interface, which is attributed to the surface roughness and porosity.[36] W1 represents the Warburg impedance, which
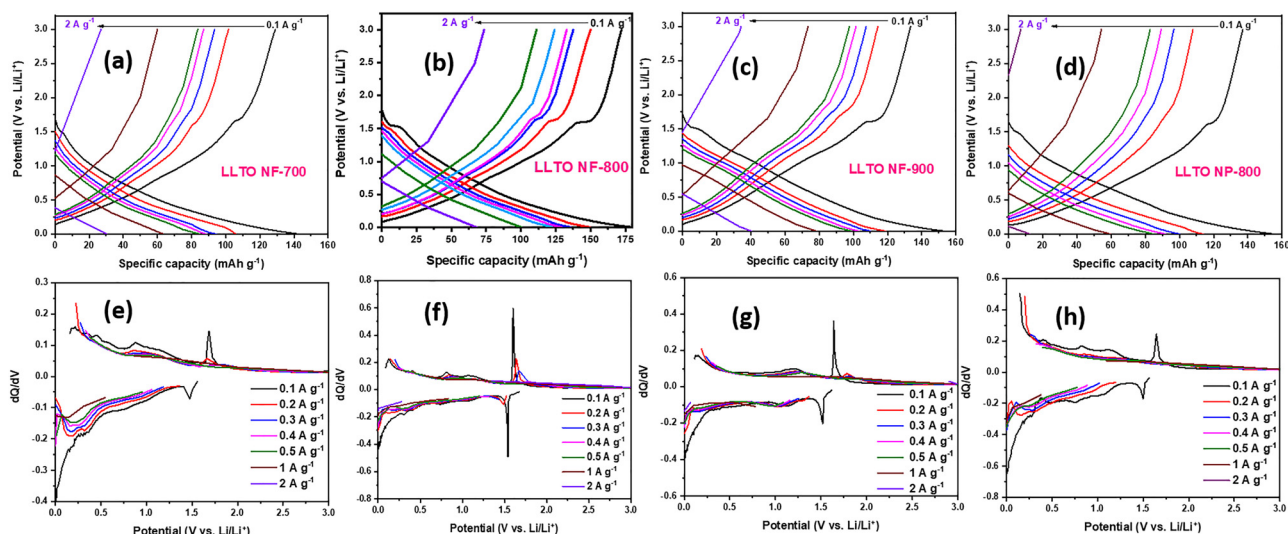

Fig. 6 GCD profiles of (a) LLTO NF-700, (b) LLTO NF-800, (c) LLTO NF-900, and (d) LLTO NP-800 at different current rates. (e)–(h) Corresponding differential capacity (dQ/dV) profiles.
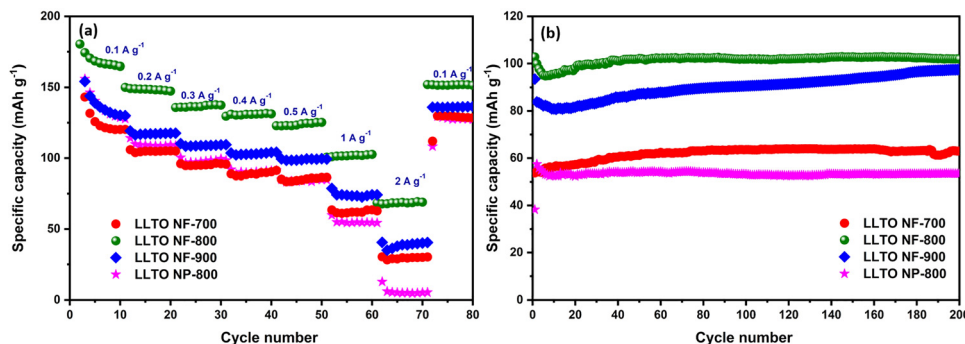
Fig. 7 (a) Rate capability and (b) cycling stability of LLTO NF-700, LLTO NF-800, LLTO NF-900, and LLTO NP-800.
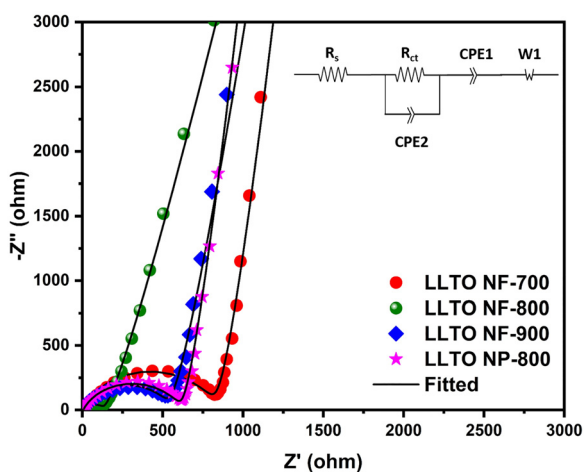

Fig. 8 Nyquist plots of LLTO NF-700, LLTO NF-800, LLTO NF-900, and LLTO NP-800 (inset: equivalent circuit).

describes Li-ion diffusion in the electrode, with a lower value indicating better ionic transport. CPE1 accounts for the SEI capacitance, which influences the charge storage and stability. The charge transfer resistance (R_{ct}) obtained from the fitting is 800 Ω, 114 Ω, 520 Ω, and 600 Ω for LLTO NF-700, LLTO NF-800, LLTO NF-900, and LLTO NP-800, respectively, indicating the best charge transfer in LLTO NF-800 electrode.

GITT was performed on the LLTO electrodes to infer the diffusion kinetics under dynamic conditions at 0.1 A g^{-1}. For the measurement, the cell was allowed to charge/discharge for 10 min, and then maintained under rest conditions for 30 min. Fig. 9a displays the GITT curves of LLTO NF-700, LLTO NF-800, LLTO NF-900, and LLTO NP-800, revealing their distinct discharge/charge voltage profiles. LLTO NF-800 exhibits the highest specific capacity (175 mAh g^{-1}), followed by LLTO NF-700 (129 mAh g^{-1}) and LLTO NF-900 (131 mAh g^{-1}), with LLTO NP-800 showing the lowest value (129 mAh g^{-1}). Fig. 9(b) and (c) present the reaction resistance during charging and discharging, respectively, as a function of capacity. LLTO NF-800 exhibited the lowest reaction resistance, indicating its superior charge transfer kinetics. LLTO NF-700 and LLTO NF-900 exhibit intermediate values, while LLTO NP-800 shows the highest value. Fig. 9(d) and (e) illustrate the lithium-ion diffusion

coefficient (log D_{Li^+}) during charge and discharge *versus* potential, respectively. LLTO NF-800 provides the highest diffusion coefficient (1.90 × 10^{-5} cm^2 s^{-1} for charge and 8.20 × 10^{-6} cm^2 s^{-1} for discharge), suggesting better lithium-ion transport. LLTO NF-700 (2.94 × 10^{-5} cm^2 s^{-1} for charge and 3.75 × 10^{-6} cm^2 s^{-1} for discharge) and LLTO NF-900 (5.86 × 10^{-5} cm^2 s^{-1} for charge, 5.67 × 10^{-6} cm^2 s^{-1} for discharge) possess slightly lower, more variable coefficients, whereas LLTO NP-800 exhibit the lowest value (6.96 × 10^{-5} cm^2 s^{-1} for charge and 4.95 × 10^{-5} cm^2 s^{-1} for discharge). Collectively, the data suggest that LLTO NF-800 has the best electrochemical performance due to its highest capacity, lowest resistance, and improved lithium-ion mobility.

The comprehensive electrochemical evaluation, encompassing cyclic voltammetry, rate capability, and cycling stability, demonstrated the superior performance of LLTO NF-800 compared to the other LLTO samples. Kinetic analysis, such as EIS and GITT, revealed that LLTO NF-800 exhibits enhanced charge transfer and a superior lithium-ion diffusion coefficient, further confirming its advantages for lithium storage. To further optimize its performance and investigate the influence of carbon additives and binders, LLTO NF-800 was modified. Ketjenblack (KB) as a carbon additive and sodium alginate (SA) as a water-based binder were incorporated. These combinations resulted in the following materials, which are designated for subsequent electrochemical analysis: LLTO-KB-SA (LLKS), LLTO with carbon black (CB) and PVDF binder (LLCP), and LLTO-KB with PVDF binder (LLKP).

3.4. Impact of carbon additives and binders on electrochemical properties of LLTO NF-800 electrode

To evaluate the role of carbon additives and binders, the electrochemical performance of the optimized LLTO NF-800 was investigated using different carbon additives, including Ketjenblack (KB) and carbon black (CB), and binders, including polyvinylidene difluoride (PVDF) and sodium alginate (SA). The obtained CV profiles of LLTO + CB + PVDF (LLCP), LLTO-KB-SA (LLKS), and LLTO-KB-PVDF (LLKP) at different scan rates are shown in Fig. 10(a)–(c), respectively. They consist of several redox peaks attributed to the multiple-phase transition of tetravalent titanium in LLTO NFs.[35] The broad reduction peak centered at 2.3 V *vs.* Li/Li$^+$ in the 1st cycle of LLCP disappeared
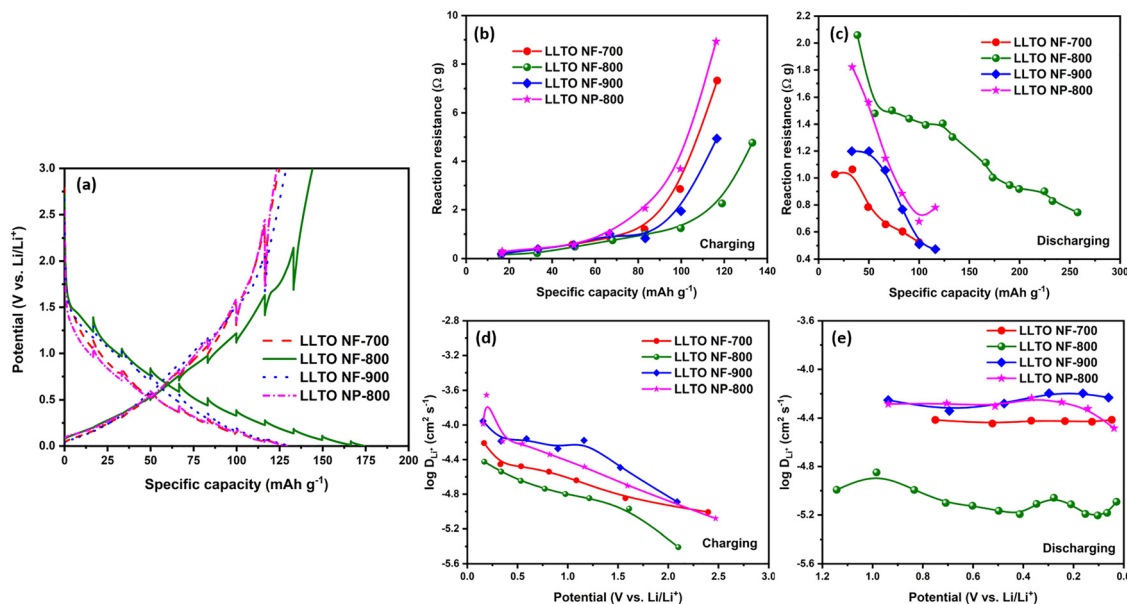
Fig. 9 (a) GITT profile of LLTO NF-700, LLTO NF-800, LLTO NF-900, and LLTO NP-800 at 0.1 A g^{-1}, (b) and (c) reaction resistance for charge and discharge, and (d) and (e) diffusion coefficient for charge and discharge of LLTO NF-700, LLTO NF-800, LLTO NF-900, and LLTO NP-800.
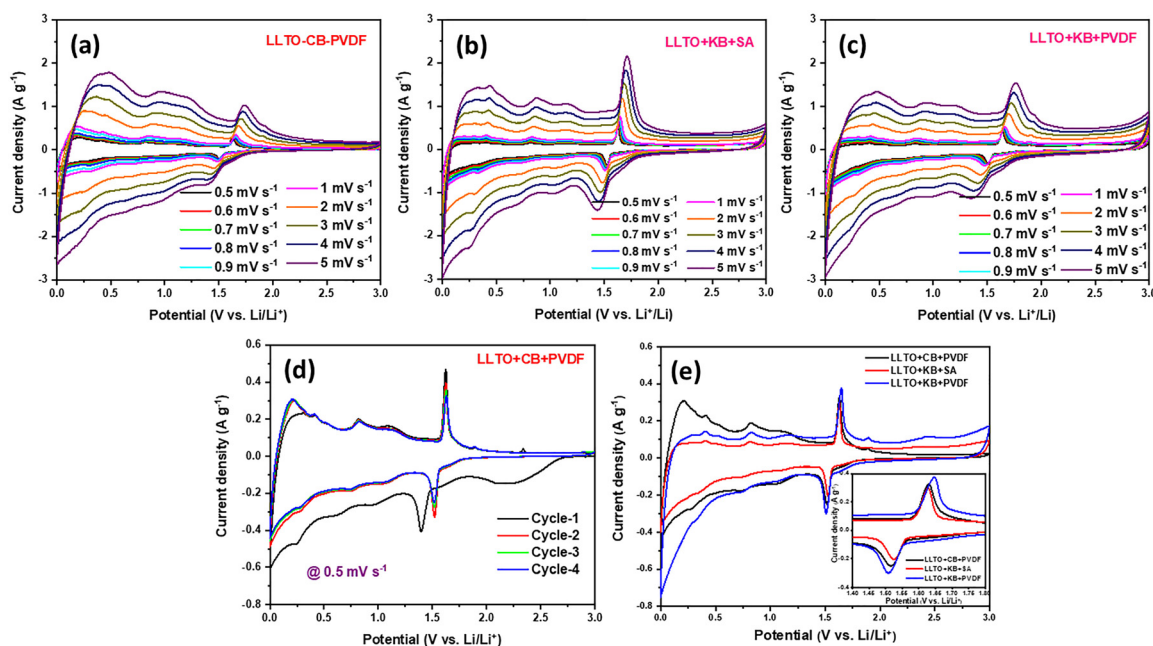

Fig. 10 (a)–(c) CV at different scan rates (0.5 to 5 mV s^{-1}) for the LLCP, LLKS, and LLKP electrodes. (d) Initial four cycles of CV at 0.5 mV s^{-1} for the LLCP electrode and (e) CV for LLCP, LLKP, and LLKS at 0.5 mV s^{-1}.

in the subsequent cycles (2 to 4) at 0.5 mV s^{-1} (Fig. 10d), corresponding to the formation of an SEI layer.[37] The obtained reduction peaks at 1.39, 0.97, 0.62, and 0.25 V vs. Li/Li$^+$ are right-shifted, representing improved kinetics after the initial cycle. The following cycles are overlaid, indicating the better reversibility of the LLTO NF. The prominent redox peaks at 1.52 and 1.63 V vs. Li/Li$^+$ are attributed to the redox reactions of Ti^{3+}/Ti^{4+}.[17] The normalized CV of LLCP, LLKB, and LLKS shown in Fig. 10e demonstrate that the peak current in the range of 1.3 to

1.8 V vs. Li/Li$^+$ follows the order of LLCP < LLKB < LLKS. This suggests that the LLKS electrode exhibits the highest current response, likely due to the higher surface area of Ketjenblack than carbon black. This dominant redox feature emerged owing to the minimal amount of Li$_2$TiO$_3$.[38] The measured peak potential difference (ΔE) (Fig. 10e) of 104 mV for LLKS is lower than that of LLCP (113 mV) and LLKP (147 mV), suggesting the nominal polarization and higher lithium-ion diffusion in the LLKS electrode. Additionally, ΔE is inversely proportional to

ionic conductivity.[39] Thus, the ionic conductivity of LLKS (electrode with low polarization) is higher than that of the LLCP and LLKB electrodes. Higher ionic conductivity is contributed by sodium alginate polymer. Given that sodium alginate is a natural ionic polymer made of sodium ions and alginate chains, it creates a more conductive matrix than the non-ionic nature of PVDF.[15] Its structure includes carboxylate groups, which interact with ions, forming a network that supports ionic conduction.[40] Additionally, the flexible and mobile polymer chains of sodium alginate enable better ion transport compared to the rigid structure of PVDF. Notably, the observed peak potential difference is lower than that of the recently reported highly stable $Li_{0.35}Nd_{0.55}TiO_3$ electrode (160 mV) measured at a high scan rate of 0.2 mV s^{-1}.[41] Additionally, all three electrodes exhibit good reversibility without significant polarization, even at a higher scan rate of 5 mV s^{-1} (Fig. 10(a)–(c)).

Moreover, CV was used to disclose the role of a Faradaic/diffusion-controlled process for Li-ion intercalation. It is well known that surface atoms contribute capacitively through the double-layer effect, while redox species in the electrode acquire a greater Faradaic contribution. The contributions are identified separately using the universal Power law (eqn (1)).[42]

$$i = a\nu^b \tag{1}$$

where i (mA) is the specific current response at a particular voltage V with the particular scan rate ν (mV s^{-1}), while a and b are adjustable parameters. According to the linear fit of log(i) $vs.$ log(ν), an accurate value of b (slope) at a fixed potential can be deduced. The current was measured at different scan rates for the dominant redox peaks (1.52 and 1.63 V $vs.$ Li/Li$^+$). Fig. 11(a)–(c) suggest that both the anodic and cathodic peak currents at scan rates of 0.1 to 1 mV s^{-1} are fitted closely to 0.6 (0.57 to 0.61) (Table 2). This suggests that a diffusion-controlled process dominates the storage mechanism. Furthermore eqn (2) is used to evaluate the quantitative contribution of diffusion and pseudocapacitance.

$$i = k_1\nu + k_2\nu^{1/2} \tag{2}$$

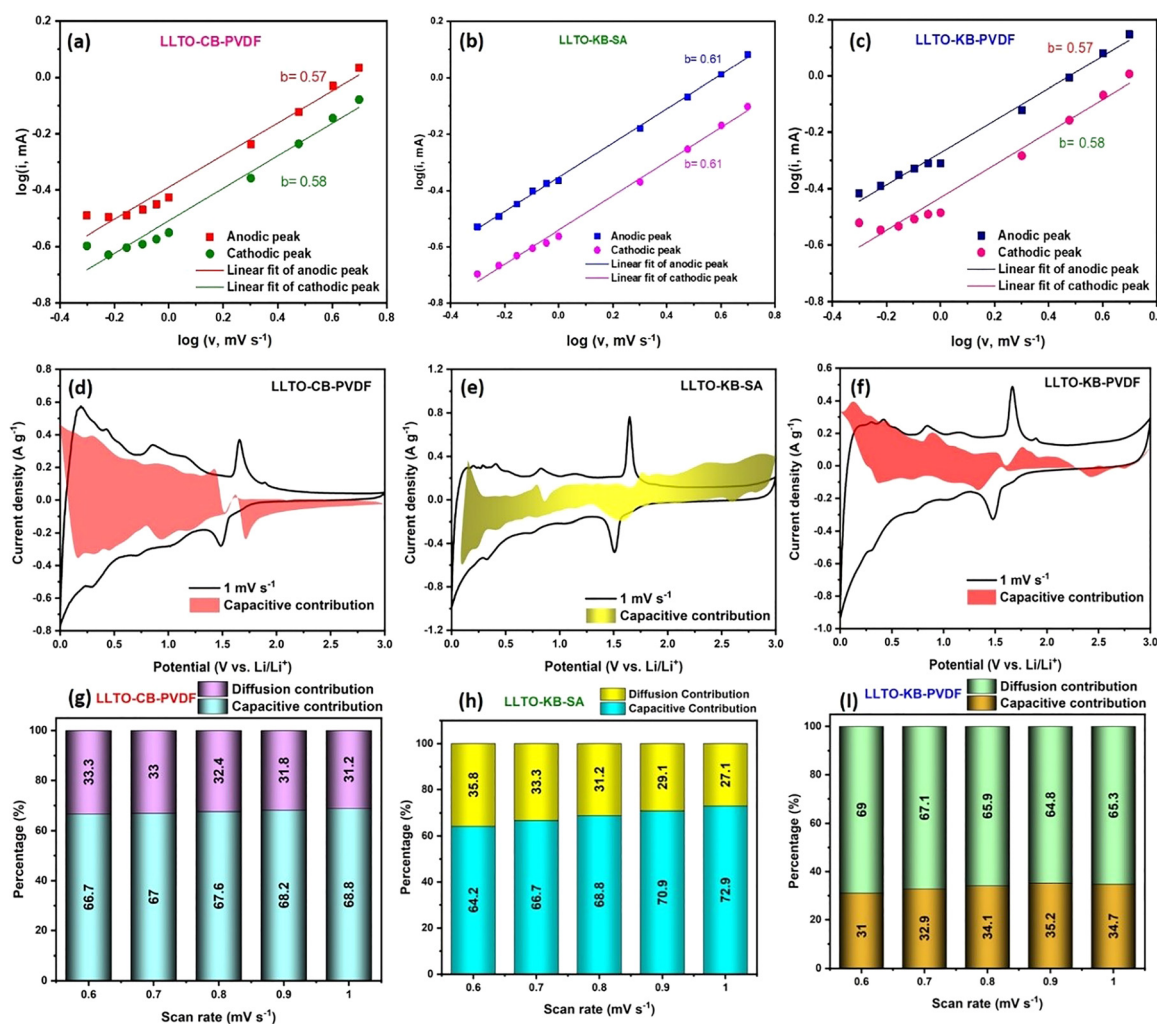

Fig. 11 (a)–(c) Plot of log(i) $vs.$ log(ν), (d)–(f) representative CV of capacitive contribution at 1 mV s^{-1}, and (g)–(i) contribution of diffusion and capacitance from 0.5 to 1 mV s^{-1} for LLCP, LLKP, and LLKS electrodes.

Table 2 b-Value for the cathodic and anodic peaks of different binders and carbon additives with LLTO NF-800
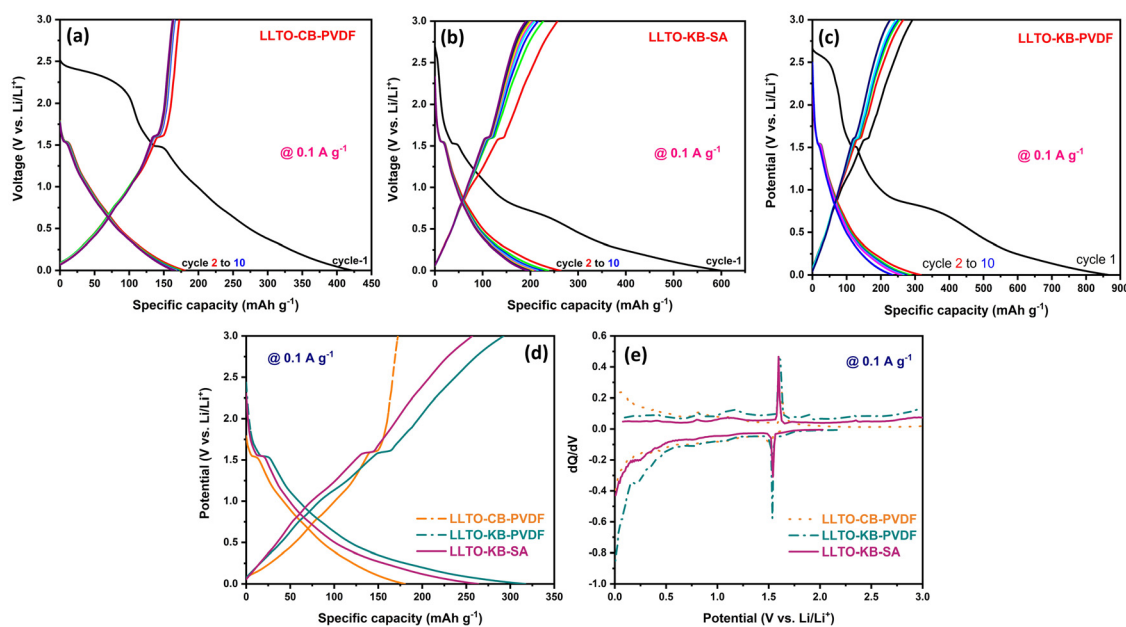
Electrode configuration	(0.5 to 5 mV s^{-1})	
	Anodic	Cathodic
LLTO-CB-PVDF	0.57	0.58
LLTO-KB-PVDF	0.57	0.58
LLTO-KB-SA	0.61	0.61

where the term $k_1\nu$ represents the diffusion-controlled contribution, whereas $k_2\nu^{1/2}$ denotes the capacitive contribution. The capacitive contributions of LLCP, LLKP, and LLKS are 66.7%, 31.04%, and 35.8% at a low scan rate of 0.6 mV s^{-1}, respectively. As a result, the diffusion contribution is 33.3%, 68.96%, and 64.2% for LLCP, LLKP, and LLKS, respectively. It has been confirmed that the LLKP electrode has a higher diffusion contribution, but LLCP has a higher capacitance contribution. As the scan rate increases, the contribution of diffusion is reduced for all the cells due to the shorter contact time for the intercalation reaction. Even at a relatively high scan rate of 1 mV s^{-1}, the diffusion process takes up 65.27% of the LLKP storage space. Based on the CV and kinetic analysis, it is evident that the LLTO electrode with Ketjenblack and sodium alginate polymer (LLKS) performed better than the LLKB and LLCP electrodes. This superior performance is demonstrated by its higher current response, minimal polarization, and slightly increased pseudo-contribution. These results are primarily due to the carbon additive and binder, which enhance the ionic conductivity, high electrochemical activity, and reversibility. A similar observation was found by Liming Ling *et al.*, where TiO$_2$ combined with sodium alginate demonstrated smaller polarization and a higher current response compared to the

TiO$_2$-PVDF anode in an Na-ion battery.[40] Another study also found that the LiFePO$_4$/C/SA system had a lower voltage differential and a higher current than the LiFePO$_4$/C/PVDF system.[43]

Fig. 12(a)–(c) show the GCD profile for the first 10 cycles of the LLTO-CB-PVDF (LLCP), LLTO-KB-SA (LLKS), and LLTO-KB-PVDF (LLKP) electrodes at a current density of 0.1 A g^{-1}. The observed plateau between 2.5 and 2 V *vs.* Li/Li$^+$ during the 1st discharge in all the combinations is attributed to the formation of SEI, and a tiny plateau located at 1.48 V *vs.* Li/Li$^+$ corresponds to the two-phase reaction. Additionally, it is evident that the initial discharge capacities of the LLCP, LLKP, and LLKS electrodes are 420, 887, and 591 mAh g^{-1}, respectively. The high initial discharge capacities of LLKP and LLKS are attributed to the higher surface area and conductivity of Ketjenblack compared to carbon black. Therefore, in addition to the intercalation mechanism, adsorption of Li ions (pseudocapacitance) occurs in the LLKP and LLKS electrodes, contributing significantly to the formation of an SEI layer. Nevertheless, as shown in the comparative GCD in Fig. 12d, the LLCP, LLKP, and LLKS electrodes deliver capacities of 180, 317, and 263 mAh g^{-1} in the 2nd discharge cycle. The Ketjenblack-based electrodes (LLKB and LLKS) delivered a higher capacity than the carbon black-based electrodes.

This improved capacity is attributed to the higher surface area, narrow pore size distribution, and excellent conductive network structure of Ketjenblack.[44,45] Likely, compared to the PVDF binder-containing electrode (LLCP and LLKP), the sodium alginate-containing electrode (LLKS) showed a superior performance due to the carboxylic polar units present in the Na-alginate polymer chain, ensuring better interfacial interaction between the binder and the LLTO electrode material, as well as the stronger adhesion between the electrode layer and

Fig. 12 (a)–(c) GCD profiles of the first 10 cycles for LLCP, LLKS, and LLKP at 0.1 A g^{-1}, (d) comparative second-cycle GCD profiles and corresponding (e) dQ/dV curves of LLCP, LLKP, and LLKS at 0.1 A g^{-1}.

the Cu substrate.[46,47] The average discharge voltage was measured in the second cycle at 0.1 A g^{-1}. The dQ/dV curve was drawn from the second cycle of the GCD profile to better understand the insertion process (Fig. 12e). All three LLTO electrode samples show similar CV profiles. The predominant peak, observed between 1.52 and 1.63 V $vs.$ Li/Li$^+$, is attributed to the Ti^{3+}/Ti^{4+} redox pair.

Fig. 13(a)–(c) shows the charge/discharge profiles of the LLCP, LLKP, and LLKS electrodes measured at different current densities from 0.1 to 2 A g^{-1}, respectively. The calculated discharge voltages for LLCP, LLKP, and LLKS are 0.60 V, 0.51 V, and 0.50 V $vs.$ Li/Li$^+$, respectively. It is apparent that the discharge voltage is safer and provides a better opportunity for achieving a high energy density,[48] given that the average discharge voltage lies between the commercially employed graphite (0.1 V $vs.$ Li/Li$^+$) and LTO (1.5 V $vs.$ Li/Li$^+$) anodes.[49] The rate capability (Fig. 13d) results show that the discharge capacity in the 10th cycle of LLCP at 0.1, 0.2, 0.3, 0.4, 0.5, 1, and 2 A g^{-1} is 165, 147, 138, 131, 125, 102, and 68 mAh g^{-1}, respectively. The recovery percentages of the LLCP, LLKP, and LLKS electrodes in the 80th cycle compared to the second discharge cycle are 83.6%, 92.9%, and 103.3%, respectively. This suggests that LLTO NFs are quite stable during (de)intercalation. The electrochemical activation induced by the binder may contribute to the LLKS electrode achieving a maximum recovery percentage of 103.3%. As a result, the same electrode (LLKS) showed higher performance (92 mAh g^{-1}) at a higher current rate (2 A g^{-1}). In continuation of the rate performance study, the cells were allowed to run for an additional 1000 cycles. The LLCP electrode maintain the discharge capacity of 97 mAh g^{-1} over 1000 cycles. Although the LLKP electrode delivered a higher discharge capacity of

approximately 143 mAh g^{-1}, the capacity decreased drastically throughout the cycles. This may be because the high surface area carbon additive initially provides an enhanced discharge capacity; nevertheless, the larger surface area leads to reduced stability due to frequent lithium intercalation and deintercalation.[50] The unaltered capacity over 1000 cycles for LLCP is because of the dominant capacitance contribution. In contrast, diffusion contributes to the poor stability of LLKP, leading to repeated Li-ion intercalation. Furthermore, the LLKS electrode has a nominal discharge capacity of 120 mAh g^{-1} during the first few cycles, which is enhanced to 500 cycles. According to Table 3, it can be understood that the electrochemical performance of LLKS is comparable to that of previously reported electrodes prepared using high-temperature synthesis techniques. It demonstrated an improved electrochemical performance using a lower temperature and a less time-consuming method.

To comprehend the Li$^+$ diffusion kinetics of LLTO with different binders and conductive additives, EIS and GITT were employed. EIS was recorded at OCV for the LLCP, LLKS, and LLKP electrodes at frequencies ranging from 1 MHz to 1 mHz with a perturbation voltage of 10 mV. The typical EIS spectra (Fig. 14a) of all the electrodes showed a high-frequency semicircle and a low-frequency spike. The corresponding equivalent circuit (inset of Fig. 14a) and the depicted values are listed in Table 4. The solution resistance (R_s) for LLCP, LLKP, and LLKS is 12 Ω, 11 Ω, and 10 Ω, respectively. LLCP showed a lower charge transfer resistance (R_{ct}) (114 Ω) compared to LLKP (156 Ω) and LLKS (240 Ω). The equivalent circuit parameters for the three electrode configurations, namely LLTO-CB-PVDF, LLTO-KB-PVDF, and LLTO-KB-SA, reveal important insights into their electrochemical performance. The solution resistance
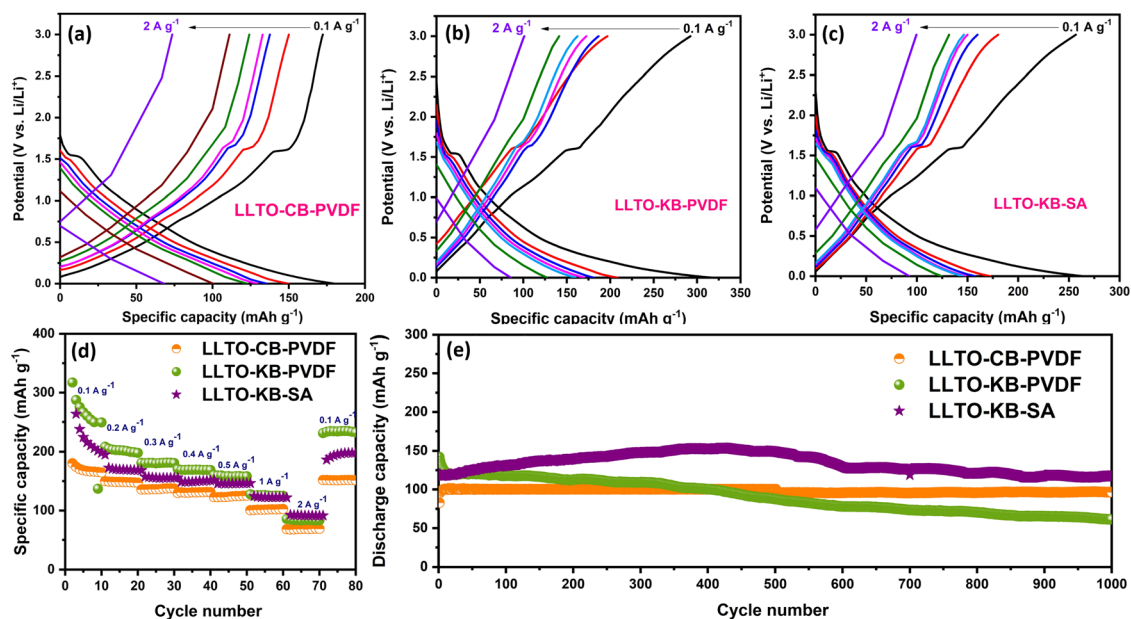

Fig. 13 GCD profiles of (a) LLCP, (b) LLKP, and (c) LLKS at different current rates. (d) Rate capability and (e) cycling stability of LLCP, LLKP, and LLKS electrodes at 1 A g^{-1}.

Table 3 Comparison of the electrochemical features of different LLTO samples

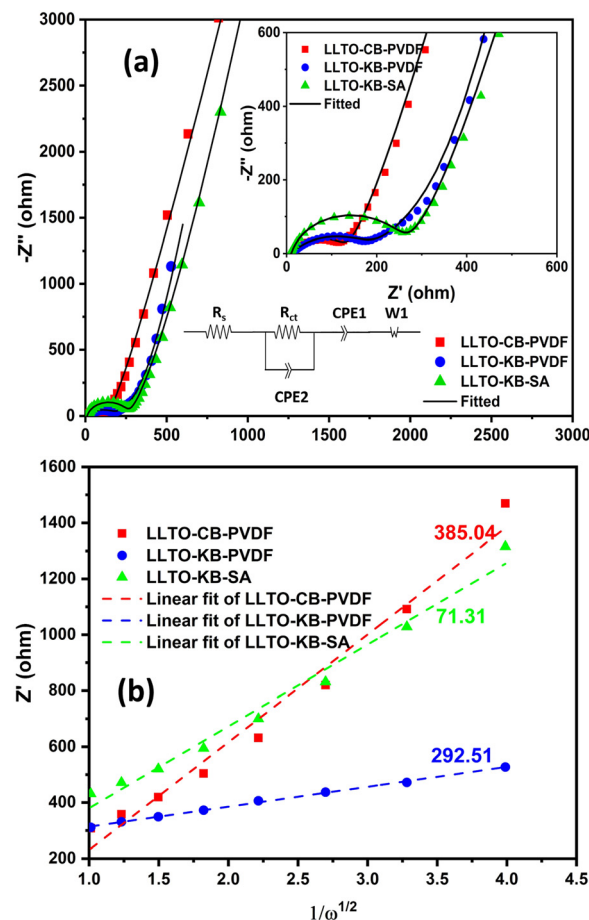| Material	Voltage window (V vs. Li/Li⁺)	Synthesis method/calcination conditions	Binder/carbon additive	Electrolyte	Initial discharge capacity (mA h g⁻¹)	Specific capacity/current density	Cycling stability (no.)	Ref.
$Li_{0.37}La_{0.5}TiO_{2.94}$	0 to 0.8	Solid state/800 °C for 4 h and 1150 °C for 12 h twice in air.	—	1 M LiClO₄ (PC)	—	12 mAh g⁻¹/0.34 mA g⁻¹	—	16
$La_{0.55}Li_{0.35}TiO_3$	0 to 2.5	Solid state/1100 °C (12 h)-air atmosphere	PVDF/acetylene black	1 M-LiPF₆ (EC/DEC)	445 to 676	160 mA h g⁻¹/0.0625 mA cm⁻²	—	51
$Li_{0.27}La_{0.54}TiO_{2.945}$	0.01 to 2.0	Sol–gel/500 °C for 5 h and 1000 °C for 10 h twice in air.	PVDF/carbon black	—	234	145 mAh g⁻¹/0.05 mA cm⁻²	50	17
$Li_{0.5}La_{0.5}TiO_3$	0 to 3	Solid state/800 °C for 8 h and 1250 °C for 12 h in air.	CMC/Ketjenblack	1 M-LiPF₆ (EC/DMC/EMC)	449	225 mAh g⁻¹/0.1 C (20 mA g⁻¹)	3000	9
$Li_{0.2375}La_{0.5875}TiO_3$	0 to 3	Solid state/800 °C for 8 h and 1150 °C for 12 h in air.	PVDF/carbon black	1 M-LiPF₆ (EC/DMC)	552.3	270 mAh g⁻¹/100 mA g⁻¹	1000	18
$Li_{0.5}La_{0.5}TiO_3$	0 to 2.5	Two-step calcination (800 °C– 8 h then 1150 °C–12 h)	PVDF/Super P	1 M-LiPF₆ (EC/DMC)	—	96. 24 mAh g⁻¹/0.5C	—	11
LLTO-CNF	0.01 to 3	Electrospinning (900 °C–3 h)	PVDF/Super P	1 M-LiPF₆ (EC/DEC)	—	250 mAh g⁻¹/0.2C	1000 (86%)	23
$Li_{0.33}La_{0.55}TiO_3$/Li_2TiO_3	0 to 3 V vs. Li/Li⁺	Electrospinning (800 °C–3 h)	PVDF/CB / PVDF/KB / SA/KB	1 M-LiPF₆ (EC/DMC)	420 / 887 / 591	180 mAh g⁻¹/100 mA g⁻¹ / 317 mAh g⁻¹/100 mA g⁻¹ / 263 mAh g⁻¹/100 mA g⁻¹	1000	Our work

Fig. 14 (a) EIS spectra (inset: zoomed view) and (b) linear fit of Z' vs. $1/\omega^{1/2}$ for LLCP, LLKP, and LLKS electrodes.

Table 4 Equivalent circuit–fitted parameters for LLCP, LLKP, and LLKS at OCV

Electrode	LLTO-CB-PVDF	LLTO-KB-PVDF	LLTO-KB-SA
R_s (Ω)	12	11	10
R_{ct} (Ω)	114	156	240
R_{CEI} (Ω)	—	170	—
W1	68	34	140
CPE1(F)	0.00199	0.01009	0.003304
CPE2(F)	4.838×10^{-5}	0.005005	1.89×10^{-5}

(R_s) is lowest for LLTO-KB-SA (10 Ω), indicating superior electrolyte conductivity, while R_{ct}, which is associated with the charge transfer resistance, is the highest for LLTO-KB-PVDF (156 Ω), suggesting slower charge transfer kinetics in this configuration. LLTO-KB-SA also shows a higher Warburg coefficient (140), indicating more restricted ion diffusion compared to the other configurations. In terms of capacitive behavior, LLTO-KB-PVDF has a high CPE1 value, implying a significant capacitive contribution at the electrode/electrolyte interface, which can enhance the charge storage. These parameters collectively suggest that LLTO-KB-SA may have advantages in terms of electrolyte conductivity and interfacial capacitance, although diffusion limitations could impact its overall
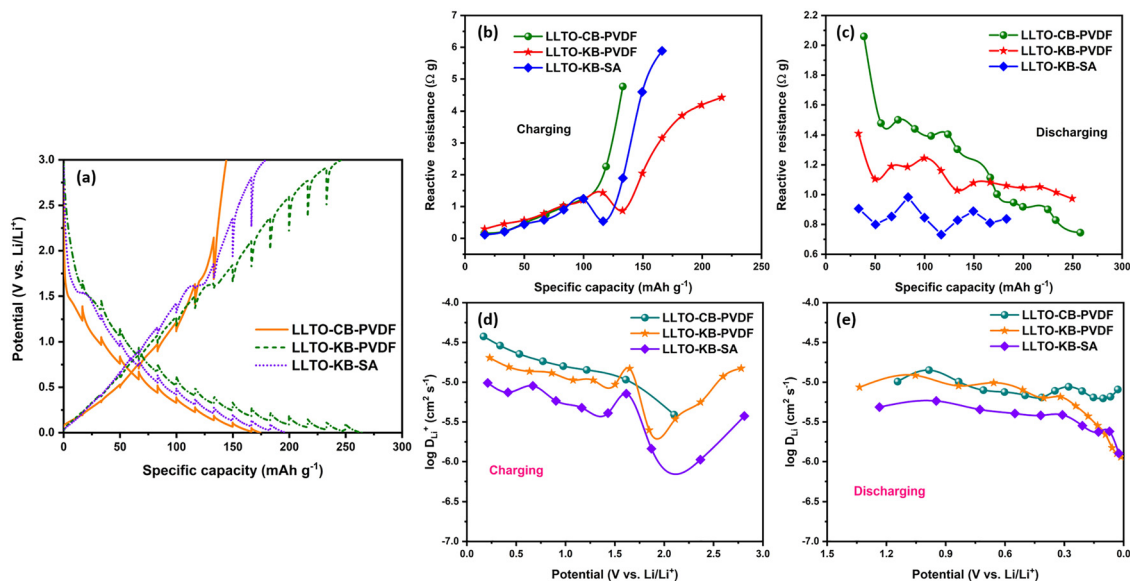
Fig. 15 (a) GITT profiles of LLCP, LLKP, and LLKS at 0.1 A g^{-1}. (b) and (c) Reaction resistance for charge and discharge and (d) and (e) diffusion coefficient for charge and discharge of LLCP, LLKP, and LLKS electrodes.

performance. The obtained diffusion coefficients from the Z' vs. $1/\omega^{1/2}$ plot (Fig. 14b) for LLCP, LLKP, and LLKS are 1.85×10^{-6}, 3.21×10^{-6}, and 5.41×10^{-5} cm^2 s^{-1}, respectively. Thus, although LLCP exhibits a lower solution resistance, LLKS showed a prominent diffusion coefficient, in accordance with the CV results. It is established that the polarization of the electrode, measured by ΔE, is inversely related to the ionic conductivity.[39] Hence, according to the measurement ΔE, it is inferred that the ionic conductivity of LLKS is superior to that of LLKP and LLCP. The lower polarization/higher ionic conductivity is possibly attained by the presence of carboxyl and hydroxyl-rich groups in the sodium alginate binder.

To further examine the diffusion process during lithiation and de-lithiation, GITT was used. It was programmed with a 10-min charge and 30-min rest condition at a current density of 0.1 A g^{-1} to measure the overpotential, reaction resistance, and diffusion coefficient. Fig. 15a shows the GITT profiles of the LLCP, LLKP, and LLKS electrodes. The specific capacities derived from GITT follow the order of LLKP > LLKS > LLCP. In the case of all LLTO electrodes, the discharge overpotential decreased as the state of charge (SOC) increased. The diffusion process is more feasible (with less diffusion length) and has a lower potential. This is reflected in the reaction resistance, given that the observed overpotential is proportional to the reaction resistance (Fig. 15(b) and (c)). The average reaction resistance for discharge follows the order of LLKS (0.85 Ω g) < LLKP (1.12 Ω g) < LLCP (1.22 Ω g). The low reaction resistance of LLKS can be attributed to its low electrolyte resistance, efficient surface charge transfer, or rapid ionic diffusion. The Li$^+$ diffusion coefficient is calculated according to Fick's second law (eqn (3)).[52]

$$D_{Li^+} = \frac{4}{\pi\tau}\left(\frac{m_B V_m}{M_B S}\right)^2\left(\frac{\Delta E_s}{\Delta E_\tau}\right)^2 \quad (3)$$

where τ is the time duration for the current pulse, m_B represents the active mass of the electrode, M_B is the molar mass of the active material, and S corresponds to the contact area of the electrode to the electrolyte. V_m symbolizes the molar volume of LLTO. ΔE_s and ΔE_τ are the changes in the potential of a constant current pulse and the equilibrium potential, respectively. Fig. 15(d) and (e) show the values of diffusion acquired during charge and discharge at different potentials.

According to Table 5, the average diffusion coefficients during the charge and discharge process of LLCP are 1.90×10^{-5} cm^2 s^{-1} and 8.20×10^{-6} cm^2 s^{-1}, respectively, which are relatively lower than that of the other compositions. More importantly, the diffusion coefficient determined from EIS and GITT is in the order of 10^{-6} cm^2 s^{-1}, which is a much higher value than that previously reported for intercalation-type anodes including Li$_4$Ti$_5$O$_{12}$ (10^{-13} to 10^{-16} cm^2 s^{-1}),[53] Ru$_{0.01}$Ti$_{0.99}$Nb$_2$O$_7$ ($\sim 10^{-15}$ cm^2 s^{-1}),[54] Li$_3$VO$_4$ (10^{-11} to 10^{-12} cm^2 s^{-1}),[55] Li$_{0.5-3x}$Pr$_{0.5+x}$TiO$_3$ ($\sim 10^{-12}$ cm^2 s^{-1}),[48] Li$_{0.5}$La$_{0.5}$TiO$_3$ (10^{-10} to 10^{-11} cm^2 s^{-1}),[9] and V$_3$O$_5$ ($\sim 10^{-9}$ cm^2 s^{-1}).[56] A higher diffusion rate indicates faster diffusion kinetics, which is advantageous for electrochemical storage. This improved diffusion coefficient is derived from the intrinsic strong ionic conductivity and electronic conductivity arising from the weak binding electron ability of Ti^{3+} in LLTO NFs.[9]

Table 5 Average diffusion coefficients from GITT analysis

Electrode	D_{Li^+} (Charge), cm^2 s^{-1}	D_{Li^+} (Discharge), cm^2 s^{-1}
LLTO-CB-PVDF	1.90×10^{-5}	8.20×10^{-6}
LLTO-KB-PVDF	1.13×10^{-5}	5.59×10^{-6}
LLTO-KB-SA	5.43×10^{-5}	3.58×10^{-6}

3.5. Postmortem analysis of LLTO electrodes

An *ex situ* examination was conducted to investigate the structural changes in the electrodes after 1000 charge–discharge cycles. Therefore, the cycled cells were disassembled, and the anodes were carefully separated and cleaned using dimethyl carbonate (DMC) solvent to remove any residual electrolyte or reaction byproducts. The *ex situ* XRD patterns were collected for three different electrode systems, including LLCP, LLKP, and LLKS. The XRD patterns (Fig. 16(a) and (b)) demonstrated no significant peak shifts or alterations in the diffraction patterns, indicating that the crystal structure of the LLTO nanofibers remained highly stable after cycling, regardless of the choice of binder or carbon additive.

The absence of phase transitions or structural degradation highlights the robustness of LLTO as a durable anode material. In addition to confirming the stability of the LLTO phase, the XRD data revealed several extra strong peaks at 43°, 51°, and 74°, which correspond to the (111), (200), and (220) planes of the Cu current collector substrate, respectively. These peaks are

Table 6 Lattice parameters and unit cell volumes of the LLTO-based cycled cells after 1000 cycles compared with those of the pristine LLTO material

Material	a (Å)	c (Å)	V (Å³)	% volume expansion
LLTO NF	3.882(1)	7.785(5)	117.3(2)	—
LLTO-CB-PVDF	3.898(6)	7.78(2)	118.1(7)	0.7
LLTO-KB-PVDF	3.888(5)	7.81(2)	118.1(6)	0.7
LLTO-KB-SA	3.898(8)	7.77(3)	118.1(9)	0.7

unrelated to the active material and arise from the metallic Cu substrate, which remains intact during the electrochemical cycling process. Importantly, the unit cell parameters of the LLTO phase after 1000 cycles, derived from full-profile Rietveld refinement, were found to be nearly identical to those of the as-prepared LLTO NFs, as shown in Table 6. This observation further reinforces the structural integrity of LLTO, confirming that it experiences minimal distortion or strain even after prolonged cycling. One of the critical findings of this study was that all the electrodes, including LLCP, LLKP, and LLKS, exhibited a volume expansion of less than 1%, specifically around 0.7%, after 1000 cycles. This minimal expansion underscores the nearly strain-free nature of the LLTO nanofibers, a property that is highly desirable in electrode materials for long-term cycling stability. The low volume change suggests that LLTO is capable of accommodating lithium-ion intercalation and de-intercalation without undergoing significant mechanical deformation, which can often lead to capacity fading or structural failure in other materials. The stability of the LLTO phase, coupled with its low expansion, makes it an excellent candidate for applications requiring long cycle life and mechanical resilience, such as high-performance lithium-ion batteries.

The enhanced electrochemical performance observed in the LLKP and LLKS electrodes, particularly in terms of faster diffusion and charge transfer rates, can be attributed to the specific properties of Ketjenblack and sodium alginate. Ketjenblack and sodium alginate form a conductive network, which significantly reduces the internal resistance and enhances the overall conductivity of the electrode, leading to improved rate capabilities and faster charge–discharge cycles. Additionally, the use of sodium alginate as a binder in the LLKS electrode offers distinct advantages due to its strong adhesive properties, which stem from the presence of carboxylic polar groups in its molecular structure.[57,58] These polar groups enhance the adhesion between the active material, conductive additives, and the current collector, resulting in improved mechanical integrity and preventing electrode delamination during cycling. Furthermore, the combination of Ketjenblack and sodium alginate in the LLKS electrode enhances the structural integrity and improves the ionic conductivity by promoting the uniform dispersion of the conductive carbon throughout the electrode matrix. This, in turn, facilitates more efficient lithium-ion diffusion, minimizes polarization, and enhances the overall performance of the electrode during cycling.[43,57]
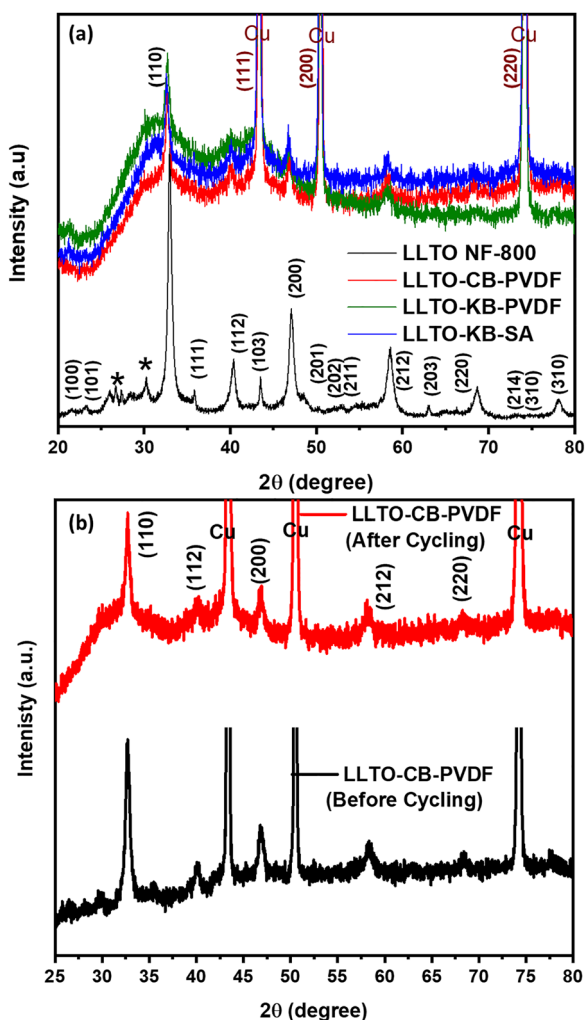

Fig. 16 (a) *Ex situ* XRD patterns of the LLCP, LLKP, and LLKS electrodes compared with the as-prepared LLTO and (b) comparison of the XRD patterns of the LLCP electrode before and after cycling.
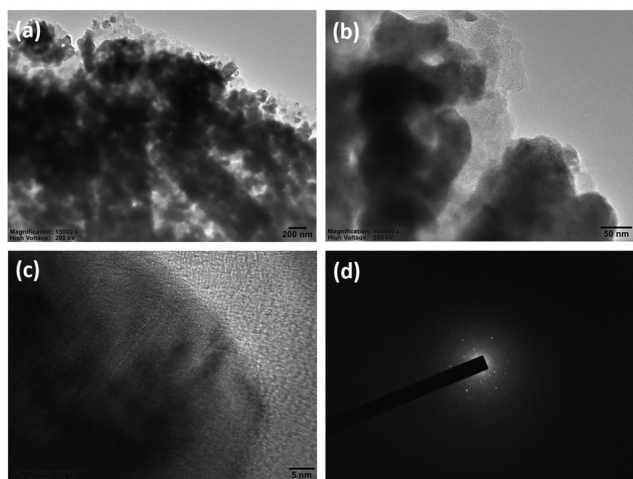
Fig. 17 (a)–(c) *Ex situ* HR-TEM images and (d) SAED pattern of the LLKS electrode after 1000 cycles.

The superior performance of LLKP and LLKS compared to the conventional LLCP electrode highlights the synergistic effect of Ketjenblack and sodium alginate, which together optimize both the electronic and ionic pathways within the electrode. This dual improvement in charge transport mechanisms makes the LLKP and LLKS systems more suitable for high-power applications, where fast charging and long cycle life are essential. Overall, the *ex situ* analysis after 1000 cycles confirms that the structural stability and mechanical resilience of the LLTO nanofibers remain uncompromised across different electrode formulations. These findings suggest that LLTO-based electrodes, particularly when combined with advanced additives such as Ketjenblack and sodium alginate, have significant potential for use in next-generation lithium-ion batteries, where high performance, stability, and durability are crucial.

Ex situ HR-TEM was performed on the LLKS electrode after 1000 cycles to investigate its morphological changes. The HR-TEM images, as shown in Fig. 17(a)–(c), reveal the microstructure of the cycled electrode at different magnifications. The HR-TEM images, while primarily focused on morphology, suggest that the LLTO nanofibers maintain their basic structural integrity, even after extensive cycling. The SAED pattern in Fig. 17d, with its characteristic spots, confirms that the crystalline structure of LLTO remains intact. Although the TEM analysis offers localized information and might not capture all potential changes across the entire electrode, the combined XRD and HR-TEM data strongly suggest that the LLTO nanofibers in the LLKS electrode exhibit good structural and compositional stability after 1000 cycles.

4. Conclusion

The $Li_{0.33}La_{0.55}TiO_3$ (LLTO) nanofibers were synthesized *via* the electrospinning technique at different temperatures (700 °C, 800 °C, and 900 °C) and compared with LLTO nanoparticles (LLTO-NP 800) prepared by the sol–gel method. Structural analyses using XRD and Raman spectroscopy confirm the major phase of tetragonal $Li_{0.33}La_{0.55}TiO_3$ and secondary phases such as Li_2TiO_3 and $La_2Ti_2O_7$ in LLTO NFs. HR-TEM and EDS mapping reveal the uniform distribution of La, Ti, and O atoms along the one-dimensional nanofibers. Among the prepared LLTO NF, LLTO-NF 800 exhibits the most favorable electrochemical performance, as demonstrated by cyclic voltammetry, rate capability, and cycling stability tests. Kinetic analyses, including electrochemical impedance spectroscopy (EIS) and galvanostatic intermittent titration technique (GITT), indicate that LLTO-NF 800 possesses enhanced charge transfer and a superior lithium-ion diffusion coefficient $(1.90 \times 10^{-5}$ cm^2 $s^{-1})$, confirming its suitability for high-performance lithium storage. Further, different carbon additives [(carbon black (CB) and Ketjenblack (KB))] and binders such as PVDF and SA were examined with LLTO-NF 800 electrodes. The electrodes with KB and SA (LLKS) achieved the highest discharge capacity of 417 mAh g^{-1} at 0.1 A g^{-1}, the lowest reaction resistance (0.85 Ω g), and the highest diffusion coefficient $(5.43 \times 10^{-5}$ cm^2 $s^{-1})$ among the tested variants. Their better electrochemical performance is attributed to the high surface area of KB and the polar functional groups in SA, which together facilitate improved ion transport and electrode kinetics. *Ex situ* XRD analysis after 1000 cycles at 1 A g^{-1} reveals that all the LLTO-based electrodes exhibit minimal volume change (<1%), affirming their low-strain characteristics and mechanical robustness. These findings establish that LLTO nanofibers, particularly when optimized with appropriate conductive additives and binders, are attractive anode candidates for durable, high-rate lithium-ion batteries.

Conflicts of interest

There are no conflicts to declare.

Data availability

Most of the data are provided directly in the manuscript or supplementary information (SI). Supplementary information is available. See DOI: **https://doi.org/10.1039/d5ya00211g**.

All other data are available upon request.

Acknowledgements

References

1 J. P. Pender, G. Jha, D. H. Youn, J. M. Ziegler, I. Andoni, E. J. Choi, A. Heller, B. S. Dunn, P. S. Weiss, R. M. Penner and C. B. Mullins, *ACS Nano*, 2020, **14**, 1243–1295.

2 M. H. Hossain, M. A. Chowdhury, N. Hossain, M. A. Islam, M. H. Mobarak, M. Hasan and J. Khan, *Chem. Eng. J. Adv.*, 2024, **17**, 100588.

3 M. H. Hossain, M. A. Chowdhury, N. Hossain, M. A. Islam and M. H. Mobarak, *Chem. Eng. J. Adv.*, 2023, **16**, 100569.

4 Z. Liu, Y. Huang, Y. Cai, X. Wang, Y. Zhang, Y. Guo, J. Ding and W. Cheng, *ACS Appl. Mater. Interfaces*, 2021, **13**, 18876–18886.

5 L. Yan, J. Qin, B. Liang, S. Gao, B. Wang, J. Cui, A. Bolag and Y. Yang, *Small*, 2022, **18**, 1–12.

6 N. Peng, X. Cheng, H. Yu, H. Zhu, T. Liu, R. Zheng, M. Shui, Y. Xie and J. Shu, *Energy Storage Mater.*, 2019, **21**, 297–307.

7 Z. Li, D. Yu, J. Xie, F. Tian, D. Lei and C. Wang, *ACS Appl. Mater. Interfaces*, 2024, **16**, 30055–30067.

8 G. Liang, L. Yang, Q. Han, G. Chen, C. Lin, Y. Chen, L. Luo, X. Liu, Y. Li and R. Che, *Adv. Energy Mater.*, 2020, **10**, 1904267.

9 L. Zhang, X. Zhang, G. Tian, Q. Zhang, M. Knapp, H. Ehrenberg, G. Chen, Z. Shen, G. Yang, L. Gu and F. Du, *Nat. Commun.*, 2020, **11**, 1–8.

10 A. Okos, C. F. Ciobota, A. M. Motoc and R. R. Piticescu, *Materials*, 2023, **16**, 7088.

11 B. Ma'dika, R. D. Pravitasari, R. Tasomara, A. U. Hapsari, Damisih, S. Rahayu, H. Yuliani, O. P. Arjasa, N. Herdianto, Y. Deni, Suyanti, A. Z. Syahrial, M. R. Somalu and J. Raharjo, *Int. J. Integr. Eng.*, 2022, **14**, 138–145.

12 J. Entwistle, R. Ge, K. Pardikar, R. Smith and D. Cumming, *Renewable Sustainable Energy Rev.*, 2022, **166**, 112624.

13 J. Hu, Y. Wang, D. Li and Y. T. Cheng, *J. Power Sources*, 2018, **397**, 223–230.

14 L. Zhang, X. Wu, W. Qian, K. Pan, X. Zhang, L. Li, M. Jia and S. Zhang, *Exploring More Functions in Binders for Lithium Batteries*, Springer Nature Singapore, 2023, vol. 6.

15 Y. Wang and Y. Lu, *Ind. Eng. Chem. Res.*, 2023, **62**, 11279–11304.

16 O. Bohnke, C. Bohnke and J. L. Fourquet, *Solid State Ionics*, 1996, **91**, 21–31.

17 C. Hua, X. Fang, Z. Wang and L. Chen, *Electrochem. Commun.*, 2013, **32**, 5–8.

18 K. Dai, Q. Wang, Y. Xie, M. Shui and J. Shu, *J. Mater. Sci.*, 2022, **57**, 2825–2838.

19 L. Zhang, L. Xu, Y. Nian, W. Wang, Y. Han and L. Luo, *ACS Nano*, 2022, **16**, 6898–6905.

20 J. W. Yang, H. R. Kwon, J. H. Seo, S. Ryu and H. W. Jang, *RSC Appl. Interfaces*, 2024, **1**, 11–42.

21 M. Yanilmaz, L. Chen, H. Cheng, K. E. Lee and J. Kim, *ACS Omega*, 2024, **9**, 24665–24673.

22 L. Ji, Z. Lin, A. J. Medford and X. Zhang, *Carbon*, 2009, **47**, 3346–3354.

23 N. Zheng, C. Zhang, Y. Lv, L. Cheng, L. Yao and W. Liu, *ACS Appl. Mater. Interfaces*, 2022, **14**, 11330–11338.

24 A. Lakshmi Narayana, M. Dhananjaya, N. Guru Prakash, O. M. Hussain and C. M. Julien, *Ionics*, 2017, **23**, 3419–3428.

25 L. Lv, H. D. Yang, H. Fan, L. Yang, Q. W. Chen and J. P. Zhou, *J. Environ. Chem. Eng.*, 2022, **10**, 108088.

26 A. I. Ruiz, M. L. López, M. L. Veiga and C. Pico, *J. Solid State Chem.*, 1999, **148**, 329–332.

27 D. Tirupathi Swamy, K. Ephraim Babu and V. Veeraiah, *Bull. Mater. Sci.*, 2013, **36**, 1115–1119.

28 S. Stramare, V. Thangadurai and W. Weppner, *J. Cheminf.*, 2003, **34**, 3974–3990.

29 A. Deschanvres, B. Raveau and Z. Sekkal, *Mater. Res. Bull.*, 1971, **6**, 699–704.

30 J. Ibarra, A. Várez, C. León, J. Santamaría, L. M. Torres-Martínez and J. Sanz, *Solid State Ionics*, 2000, **134**, 219–228.

31 N. S. P. Bhuvanesh, O. Bohnke, H. Duroy, M. P. Crosnier-Lopez, J. Emery and J. L. Fourquet, *Mater. Res. Bull.*, 1998, **33**, 1681–1691.

32 M. Romero, R. Faccio, S. Vázquez, S. Davyt and Á. W. Mombrú, *Ceram. Int.*, 2016, **42**, 15414–15422.

33 Y. Huang, Y. Jiang, Y. Zhou, X. Liu, X. Zeng and X. Zhu, *Ionics*, 2021, **27**, 145–155.

34 S. L. Fernandes, G. Gasparotto, G. F. Teixeira, M. A. Cebim, E. Longo and M. A. Zaghete, *Ceram. Int.*, 2018, **44**, 21578–21584.

35 B. Gu, C. Zhan, B. H. Liu, G. Wang, Q. Zhang, M. Zhang and Z. Shen, *Dalton Trans.*, 2022, **51**, 7076–7083.

36 E. H. Balaguera and A. Allagui, *JEnergy Storage*, 2024, **90**, 111801.

37 H. Sonoki, M. Matsui and N. Imanishi, *J. Electrochem. Soc.*, 2019, **166**, A3593–A3598.

38 Y. Liu, W. Li and X. Zhou, *RSC Adv.*, 2019, **9**, 17835–17840.

39 V. V. N. Phanikumar, V. R. Rikka, B. Das, R. Gopalan, B. V. Appa Rao and R. Prakash, *Ionics*, 2019, **25**, 2549–2561.

40 L. Ling, Y. Bai, Z. Wang, Q. Ni, G. Chen, Z. Zhou and C. Wu, *ACS Appl. Mater. Interfaces*, 2018, **10**, 5560–5568.

41 H. Liu, J. Xiao, H. He, K. Cao, Y. Li, B. Pan and C. Chen, *Nano Energy*, 2024, **119**, 109065.

42 B. Zou, T. Wang, S. Li, R. Kang, G. Li, S. A. El-Khodary, D. H. L. Ng, X. Liu, J. Qiu, Y. Zhao, J. Lian and H. Li, *J. Energy Chem.*, 2021, **57**, 109–117.

43 Y. Ding, X. Zhong, C. Yuan, L. Duan, L. Zhang, Z. Wang, C. Wang and F. Shi, *ACS Appl. Mater. Interfaces*, 2021, **13**, 20681–20688.

44 G. Hu, X. Sun, H. Liu, Y. Xu, L. Liao, D. Guo, X. Liu and A. Qin, *Nanomaterials*, 2022, **12**, 692.

45 Z. Yang, C. R. Kim, S. Hirata, T. Fujigaya and N. Nakashima, *ACS Appl. Mater. Interfaces*, 2015, **7**, 15885–15891.

46 P. Gurunathan, P. M. Ette and K. Ramesha, *ACS Appl. Mater. Interfaces*, 2014, **6**, 16556–16564.

47 Y. Shi, X. Zhou and G. Yu, *Acc. Chem. Res.*, 2017, **50**, 2642–2652.

48 H. Liu, J. Xiao, K. Cao, N. Ren, H. He, Y. Li, J. Si, S. Zeng, B. Pan and C. Chen, *Chem. Eng. J.*, 2024, **479**, 147765.

49 P. K. Allan, N. Louvain and L. Moncondmt, *Prospect. Li-ion Batter. Emerg. Energy Electrochem. Syst.*, 2018, vol. 4, pp. 1–55.

50 J. Zheng, J. Xiao, W. Xu, X. Chen, M. Gu, X. Li and J. G. Zhang, *J. Power Sources*, 2013, **227**, 211–217.

51 C. H. Chen and K. Amine, *Solid State Ionics*, 2001, **144**, 51–57.

52 Y. C. Chien, H. Liu, A. S. Menon, W. R. Brant, D. Brandell and M. J. Lacey, *Nat. Commun.*, 2023, **14**, 2289.

53 X. Hao and B. M. Bartlett, *Adv. Energy Mater.*, 2013, **3**, 753–761.

54 C. Lin, S. Yu, S. Wu, S. Lin, Z. Z. Zhu, J. Li and L. Lu, *J. Mater. Chem. A*, 2015, **3**, 8627–8635.

55 G. Yang, B. Zhang, J. Feng, Y. Lu, Z. Wang, V. Aravindan, M. Aravind, J. Liu, M. Srinivasan, Z. Shen and Y. Huang, *J. Mater. Chem. A*, 2018, **6**, 456–463.

56 D. Chen, H. Tan, X. Rui, Q. Zhang, Y. Feng, H. Geng, C. Li, S. Huang and Y. Yu, *InfoMat*, 2019, **1**, 251–259.

57 S. Zhang, S. Ren, D. Han, M. Xiao, S. Wang and Y. Meng, *J. Power Sources*, 2019, **438**, 227007.

58 M. Srivastava, A. K. Anil and K. Zaghib, *Batteries*, 2024, **10**, 268.